

Quantifying Efficiency Limitations in All-Inorganic Halide Perovskite Solar Cells


Ye Yuan, Genghua Yan,* Ruijiang Hong, Zongcun Liang,* and Thomas Kirchartz*

While halide perovskites have excellent optoelectronic properties, their poor stability is a major obstacle toward commercialization. There is a strong interest to move away from organic A-site cations such as methylammonium and formamidinium toward Cs with the aim of improving thermal stability of the perovskite layers. While the optoelectronic properties and the device performance of Cs-based all-inorganic lead-halide perovskites are very good, they are still trailing behind those of perovskites that use organic cations. Here, the state-of-the-art of all-inorganic perovskites for photovoltaic applications is reviewed by performing detailed meta-analyses of key performance parameters on the cell and material level. Key material properties such as carrier mobilities, external photoluminescence quantum efficiency, and photoluminescence lifetime are discussed and what is known about defect tolerance in all-inorganic is compared relative to hybrid (organic–inorganic) perovskites. Subsequently, a unified approach is adopted for analyzing performance losses in perovskite solar cells based on breaking down the losses into several figures of merit representing recombination losses, resistive losses, and optical losses. Based on this detailed loss analysis, guidelines are eventually developed for future performance improvement of all-inorganic perovskite solar cells.

Y. Yuan, G. Yan, R. Hong, Z. Liang
 Institute for Solar Energy Systems
 Guangdong Provincial Key Laboratory of Photovoltaic Technology
 School of Physics
 Sun Yat-sen University
 Guangzhou 510006, P. R. China
 E-mail: ge.yan@fz-juelich.de; liangzc@mail.sysu.edu.cn

Y. Yuan, G. Yan, T. Kirchartz
 IEK5-Photovoltaik
 Forschungszentrum Jülich
 52425 Jülich, Germany
 E-mail: t.kirchartz@fz-juelich.de

T. Kirchartz
 Faculty of Engineering and CENIDE
 University of Duisburg-Essen
 Carl-Benz-Str. 199, 47057 Duisburg, Germany

 The ORCID identification number(s) for the author(s) of this article can be found under <https://doi.org/10.1002/adma.202108132>.

© 2022 The Authors. Advanced Materials published by Wiley-VCH GmbH. This is an open access article under the terms of the Creative Commons Attribution License, which permits use, distribution and reproduction in any medium, provided the original work is properly cited.

DOI: 10.1002/adma.202108132

1. Introduction

Lead-halide perovskites exhibit a range of properties that are attractive for optoelectronic and in particular photovoltaic applications. These properties include the ease of fabricating perovskite thin-films with exceptionally long charge-carrier lifetimes and a steep absorption onset leading to absorption coefficients $>10^4 \text{ cm}^{-1}$ only a few meV above the bandgap.^[1] Within the family of lead-halide perovskites the best optoelectronic properties are achieved for a range of bandgaps of around 1.5 to 1.8 eV which is a highly useful range for the application as higher-bandgap absorber in tandem or triple-junction solar cells.^[2] In this range of bandgaps, perovskites have only III–V semiconductors as viable competition,^[3] but have the advantage of substantially lower fabrication cost. While there are many direct semiconductors with good absorption and suitable bandgaps for photovoltaics,^[4] there are very few that have so low non-radiative recombination losses and such high luminescence

quantum efficiencies as lead-halide perovskites.^[5–7] This is achieved not only in single crystals but also in polycrystalline thin films.^[8] A specific reason for the good performance of these polycrystalline materials is the antibonding valence band of lead-halide perovskites that leads to shallow intrinsic defects^[9] and has earned the family of lead-halide perovskites the label “defect-tolerant semiconductor”.^[10,11] There are two key downsides of the technology that are currently standing in the way of commercialization:^[12] One is the long-term stability of the material and the other one is the use of the toxic element lead that is, however, of crucial importance for understanding the superior optoelectronic properties^[11] and is therefore difficult to replace. There are various strategies to either replace lead, reduce it or contain it safely inside the film.^[13] In terms of improving stability, one major approach of increasing importance in the community is to replace the organic cations methylammonium or formamidinium that are typically used so far with inorganic elements such as Cs.^[14] The key challenge here is that the perovskite structure (ABX_3) as shown in **Figure 1a** has to contain A-site cations of an appropriate size to stabilize the BX_6 octaeder at the core of the perovskite structure. Given the relatively large size of Pb and I or (to a lesser degree) Br, the A-site cations have to be large enough.

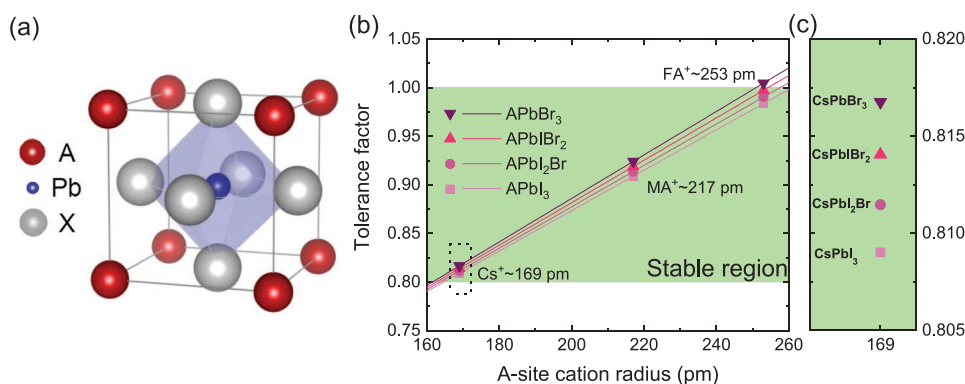


Figure 1. a) Structural diagram of APbX₃ perovskite. b) Goldschmidt tolerance factor along with A-site cation radius for APbX₃ perovskite with different X species. c) The partial enlarged details related to pure CsPbI_{3-x}Br_x perovskites. The curve and point values were calculated according to the following cation radii: Cs⁺ ≈ 169 pm,^[20] MA⁺ ≈ 217 pm,^[21] FA⁺ ≈ 253 pm,^[21] Pb²⁺ ≈ 120 pm,^[20] I⁻ ≈ 220 pm,^[20] Br⁻ ≈ 196 pm.^[20]

To decide exactly how large those cations have to be, the so-called Goldschmidt tolerance factor

$$t = \frac{(r_A + r_X)}{\sqrt{2}(r_B + r_X)} \quad (1)$$

where r_A , r_B , and r_X are the radii of the corresponding ions^[15,16] provides some orientation. If t deviates from the range of 0.8–1.0, the compositions are unlikely to form a stable perovskite phase.^[16,17] Figure 1b shows the Goldschmidt tolerance factor varying with A-site cation radius for APbI_{3-x}Br_x perovskites. Though Cs is the largest suitable element with oxidation state +I, its ionic radius is slightly too small so that Cs-based compositions with Pb and a halogen atom have tolerance factors that are at the lower end of the range of Goldschmidt factors that likely lead to the formation of a stable perovskite phase. By contrast, the MA⁺ leads to a Goldschmidt factor that is in the middle of the stable region while the FA⁺ is a bit too large leading to Goldschmidt factors at the upper end of the stable region. Mixing Cs⁺ and FA⁺ cations can lead to a more suitable tolerance factor and is frequently used in the development of efficient perovskite-based solar cell materials.^[18] In addition, from the lines shown in the figure, we can find that the tolerance factor increases when the anion changes from I⁻ to Br⁻, due to the smaller radius of Br⁻. As shown in Figure 1c, the tolerance factor of CsPbI₃ is close to 0.8, i.e., close to the lower end of the stable region making it challenging to stabilize the perovskite phase of CsPbI₃.^[19,20] By decreasing the x value, the tolerance factor t of CsPbI_{3-x}Br_x ($0 \leq x \leq 3$) increases, which is beneficial for the phase stability.

In 2012, the first all-inorganic halide perovskite solar cells with a structure of indium tin oxide (ITO)/CsSnI₃/Au/Ti were reported. However, the power conversion efficiency (PCE) was only 0.88%.^[22] In 2016, Luther and co-workers have fabricated all-inorganic perovskite solar cells based on CsPbI₃ quantum dots (QDs) with a PCE over 10%.^[23] Since this publication in Science, interest in the field of all-inorganic perovskite solar cells has been growing rapidly. As shown in Figure 2a, the numbers of published articles related to all-inorganic perovskite solar cells is steadily increasing. In 2014, only 0.7% of perovskite solar cell related papers focus on all-inorganic perovskites (based on Web of Science database). However, now in 2021,

the proportion of articles has risen up to 4.3% and it continues rising. In Figure 2b, the development of champion efficiencies varying with the accumulated number of related articles is presented. We observe that the PCE of all-inorganic perovskite solar cells has increased from 0.09% in 2014^[24] to over 20% in 2021^[25] with ≈950 published articles. This quantity of articles is close to that for the hybrid perovskite solar cells achieving 20% PCE. Moreover, from the experience of the traditional perovskite solar cells development, it is clear that improvements beyond 20% become increasingly difficult and require more additional papers per additional % efficiency (note the logarithmic x-axis in Figure 2b). Hence, while more efforts are needed to further increase efficiencies of all inorganic solar cells, it seems that the development so far did not require a substantially higher amount of work (measured in the number of accumulated publications) than for hybrid perovskites.

Up to now, the champion PCE of CsPbI₃-based PSC has reached 20.37% which was reported by Sang Il Seok's group^[25] while the optimal certified PCE is 18.3%, achieved by Yixin Zhao's group.^[26] Apart from CsPbI₃ (whose bandgap (E_g) is estimated to be ≈1.7 eV), all-inorganic perovskite solar cells based on CsPbI₂Br (E_g ≈ 1.9 eV), CsPbIBr₂ (E_g ≈ 2.1 eV) and CsPbBr₃ (E_g ≈ 2.3 eV) are rapidly developing as well. Figure 2c presents the champion PCE of all-inorganic CsPbI_{3-x}Br_x ($0 \leq x \leq 3$) perovskite solar cells as a function of time. As expected by the optimum bandgap range in the Shockley–Queisser model^[27] (see Figure 2d), the composition with the lowest bandgap, i.e., CsPbI₃, has consistently led the field in PCE, achieving 20.37% PCE,^[25] followed by 19.65%^[28] PCE for CsPbI₂Br_x ($2 < x < 3$) perovskite solar cells and 17.36%^[29] PCE for CsPbI₂Br perovskite solar cells, whereas the CsPbIBr₂ and CsPbBr₃ perovskite solar cells show relatively low PCE of 11.3%^[30] and 10.85%^[31] respectively. In addition, hybrid perovskite solar cells are shown for comparison (majority of them have been recorded in the Best Research Cell Efficiencies Chart by NREL).^[32] It can be found that the PCE of all-inorganic perovskite solar cells is still somewhat behind that of the hybrid species which have already reached 25.5%.^[32] Figure 2d depicts the champion efficiency of different solar cells and the Shockley–Queisser limit along with bandgap values. It is clear that there is still large room for efficiency improvement of all-inorganic perovskites, compared with the c-Si, GaAs and hybrid perovskite solar cells.^[33]

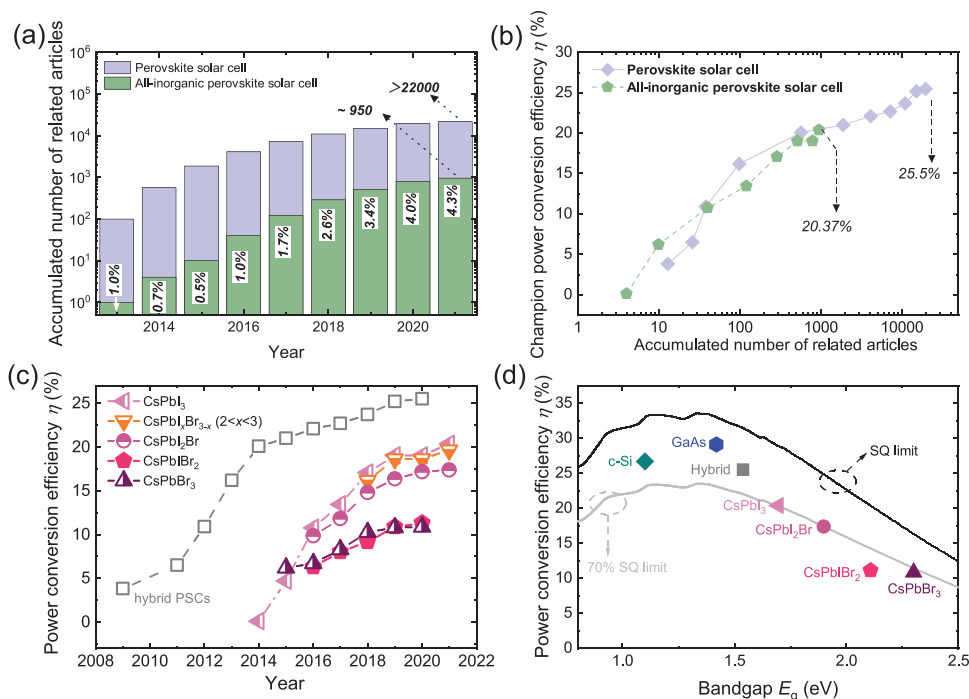


Figure 2. a) Accumulated number of related articles as a function of time for the search strings given in the legend taken from ISI Web of Science. Proportion of all-inorganic perovskite solar cells are also shown. b) Relationship between champion efficiencies and the accumulated number of related articles. c) The champion power conversion efficiencies of all-inorganic perovskite solar cells along with years. The devices are classified into 5 groups by the iodine to bromine ratio quantified via the value of x . The efficiencies of hybrid perovskite solar cells are also shown for comparison. The devices with Sn doping process are not shown in the figures, because the bandgap deviates significantly from the intrinsic values. d) The champion efficiency of different all-inorganic perovskite solar cells compared with the SQ limit. The record efficiency of c-Si, GaAs and hybrid perovskite solar cells are shown for comparison.

It should be noted that as the bandgap increases, both the efficiency limit and actual efficiency decrease. Though the PCE values of all-inorganic perovskite solar cells with high Br contents seem not pretty appealing, it is satisfying that the stability and reliability become better and better. Furthermore, if taking the thermodynamic limits into account, we can find that the η/η^{SQ} values of many all-inorganic perovskite solar cells have approached 70%, which means further performance improvement would become more difficult. Therefore, precise and reliable meta-analysis of performance losses become desiderated, which could be conducted to point out the directions for further optimization.

In the following, we will discuss the material properties of all-inorganic halide perovskites, present the typically used device geometries and then present a detailed meta-analysis of the current state of the art of this technology. The meta-analysis will focus especially on the analysis of different efficiency limitations such as recombination losses, resistive losses and optical losses.

2. Material Properties

Any solar cell absorber material has to fulfil some necessary conditions to allow its use in high-efficiency solar cells. These conditions are to have a suitable absorption coefficient, good charge transport measured via the electron and hole mobilities

as well as a long lifetime of charge carriers.^[34] The latter argument is often rephrased as having a low defect density because short lifetimes are typically related to a high defect density. In the following, we will therefore give an overview over these three properties and discuss their change with stoichiometry and bandgap as well as compare them with hybrid perovskites.

2.1. Absorption Coefficient and Bandgap

Excellent photon absorption is a precondition for perovskites to be used in optoelectronic and photovoltaic applications. Hybrid lead-halide perovskites have been shown to have fairly sharp absorption coefficients that rise quickly above the bandgap to reach values $>10^4 \text{ cm}^{-1}$ already few tens of meV above the bandgap.^[1] This allows efficient solar cells to have absorber thickness below 1 μm and still achieve sharp onsets of the quantum efficiency. For all-inorganic lead-halide perovskites comparably little data is available on the absorption coefficient. Judging from available quantum efficiency data and the typical thicknesses used for efficient devices, the absorption coefficient is likely rather similar to that of hybrid perovskites. However, more detailed studies are missing. This is true for the overall value of the absorption coefficient but also for the shape of the absorption onset and parameters such as the Urbach energy,^[63] which can be determined, e.g., from photothermal deflection spectroscopy or sensitive photocurrent spectroscopy methods

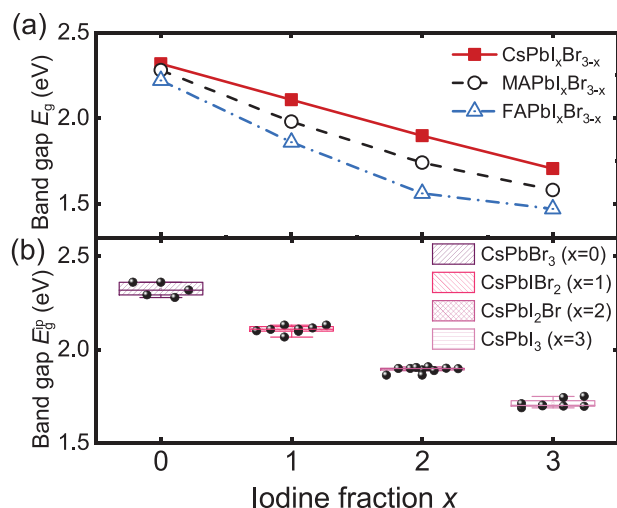


Figure 3. a) The variation of bandgap changing with x values. The E_g of FA^+ , MA^+ -containing perovskites are based on the Tauc method,^[35] while that of Cs^+ -based samples is the average value of calculated E_g^{ip} (i.e., calculated by using the inflection point of the EQE). b) The distribution of E_g^{ip} for all-inorganic perovskites. The data points are collected from relevant publications of CsPbI_3 ,^[25,26,36–41] CsPbI_2Br ,^[29,42–51] $\text{CsPbI}_2\text{Br}_2$,^[30,52–57] CsPbBr_3 ,^[58–62] of which detailed data can be found in Tables 1–5.

such as FTPS (Fourier transform photocurrent spectroscopy).^[64] Note that Urbach energies cannot reliably be determined from the frequently used UV–Vis transmission (T) & reflection (R) spectroscopy, because this method is not suitable to precisely determine low absorbance (A) values, where $A = 1 - R - T$ is close to zero and $R + T \approx 1$. In this case, small errors in R and T , will lead to large relative errors in A that prohibit a precise determination of the Urbach energy.

While there is—to our knowledge—no systematic investigation into the absolute values of the absorption coefficient or the sharpness of the absorption onset as a function of stoichiometry in the family of all inorganic perovskites, it is worth to briefly discuss the obvious change in bandgap that we have already mentioned in the context of Figure 2.

Figure 3a presents the bandgap comparison of $\text{CsPbI}_{3-x}\text{Br}_x$, $\text{MAPbI}_{3-x}\text{Br}_x$ and $\text{FAPbI}_{3-x}\text{Br}_x$ ($0 \leq x \leq 3$) varying with stoichiometric ratio of iodine. Note that the bandgap data for $\text{MAPbI}_{3-x}\text{Br}_x$ and $\text{FAPbI}_{3-x}\text{Br}_x$ come from the related references,^[35] while those for $\text{CsPbI}_{3-x}\text{Br}_x$ are calculated by EQE inflection point method.^[65] The detailed description of this method can be found in the Supporting Information (Section 1.1). It is observed that the bandgap of Cs^+ -based perovskite is wider than the MA^+ and FA^+ -based samples. Taking $x = 3$ as an example, the bandgap for CsPbI_3 , MAPbI_3 and FAPbI_3 is ≈ 1.71 eV, ≈ 1.58 eV and ≈ 1.47 eV respectively. In addition, for all the perovskite species, the bandgap decreases with increasing x values. Furthermore, with the cation changing from FA^+ , MA^+ to Cs^+ , the relation between bandgap and x value varies from nonlinear to linear. For all-inorganic perovskites, the relation could be ascribed as: $E_g^{\text{ip}} = 2.314 - 0.205x$. The distribution of E_g^{ip} for all-inorganic perovskites is shown in Figure 3b. It can be found that the E_g^{ip} of CsPbI_3 , CsPbI_2Br , $\text{CsPbI}_2\text{Br}_2$ and CsPbBr_3 is around ≈ 1.71 eV, 1.90 eV, 2.11 eV and 2.32 eV respectively, showing that varying x value of $\text{CsPbI}_{3-x}\text{Br}_x$ ($0 \leq x \leq 3$) is an

effective approach for bandgap regulation. The slight difference of E_g^{ip} in each group could be due to the fact that the bandgap of the samples would be affected by process technique, component stoichiometry, phase structure and temperature during actual preparation.

2.2. Charge-Carrier Mobilities

A further prerequisite for high photovoltaic performance is that the absorber material should have a sufficiently high mobility–lifetime product to allow efficient charge extraction before recombination happens.^[34] Depending on the exact device geometry and the presence or absence of electric fields, the mobility lifetime product may be replaced by either the diffusion length or the drift length.^[82] Thus, it is not possible to a priori state a certain minimum mobility or lifetime or even mobility–lifetime product necessary to allow efficient photovoltaic energy conversion. However, it is generally true that efficient charge transport is a necessary but not sufficient condition for any solar cell material. **Figure 4a** gives an overview over the mobility results for lead-halide perovskites. For all-inorganic components, the $\text{CsPbI}_2\text{Br}_2$ exhibit relatively lower mobilities as compared to other compositions. A possible reason could be attributed to worse film quality and higher defects density.^[70] CsPbBr_3 presents the maximum mobility value. Song et al. have prepared CsPbBr_3 single crystals (SC), achieving an attractive carrier mobility over $2000 \text{ cm}^2 \text{ V}^{-1} \text{ s}^{-1}$ measured using SCLC methods,^[77] which is the highest reported value among all-inorganic perovskites so far. As for comparison between hybrid and all-inorganic perovskites, CsPbI_3 , CsPbI_2Br and CsPbBr_3 components present competitively high mobilities if compared with FAPbI_3 - and MAPbI_3 -based samples, some of which have reported mobilities beyond $10^2 \text{ cm}^2 \text{ V}^{-1} \text{ s}^{-1}$.^[69,73,75,77] However, it should be noted that at present there are many techniques for mobility measurement, which would therefore result in difference among the reported mobility results. As shown in Figure 4b, the mobilities measured by FET, SCLC and PL-based methods generally present relatively lower values, while those determined by Hall effect measurement, time-resolved microwave current (TRMC) and THz-probe spectroscopy (OTPT) commonly show higher values. Figure 4c shows the average mobility values and standard deviations for each method. Apart from the “else” methods, the THz spectroscopy, SCLC and Hall methods always show larger fluctuations.

Possible method specific biases complicate the comparison of mobilities as a function of stoichiometry. Fortunately, some valuable comparisons of mobilities using a consistent methodology have been reported. Dastidar et al. have investigated solution-processed α - CsPbI_3 thin films via pump-probe time-resolved terahertz spectroscopy (TRTS) and revealed a charge-carrier mobility of over $30 \text{ cm}^2 \text{ V}^{-1} \text{ s}^{-1}$ and diffusion length of $\approx 1 \mu\text{m}$.^[67] The results demonstrate similar transport characteristics to literature reports of solution processed MAPbI_3 which exhibited carrier mobility and diffusion length of $35 \text{ cm}^2 \text{ V}^{-1} \text{ s}^{-1}$ and $2.5 \mu\text{m}$ via TRTS as well.^[81] Zhu et al. have investigated and made comparison of the band edge carrier properties for CsPbBr_3 , MAPbBr_3 and FAPbBr_3 macro-crystals, showing

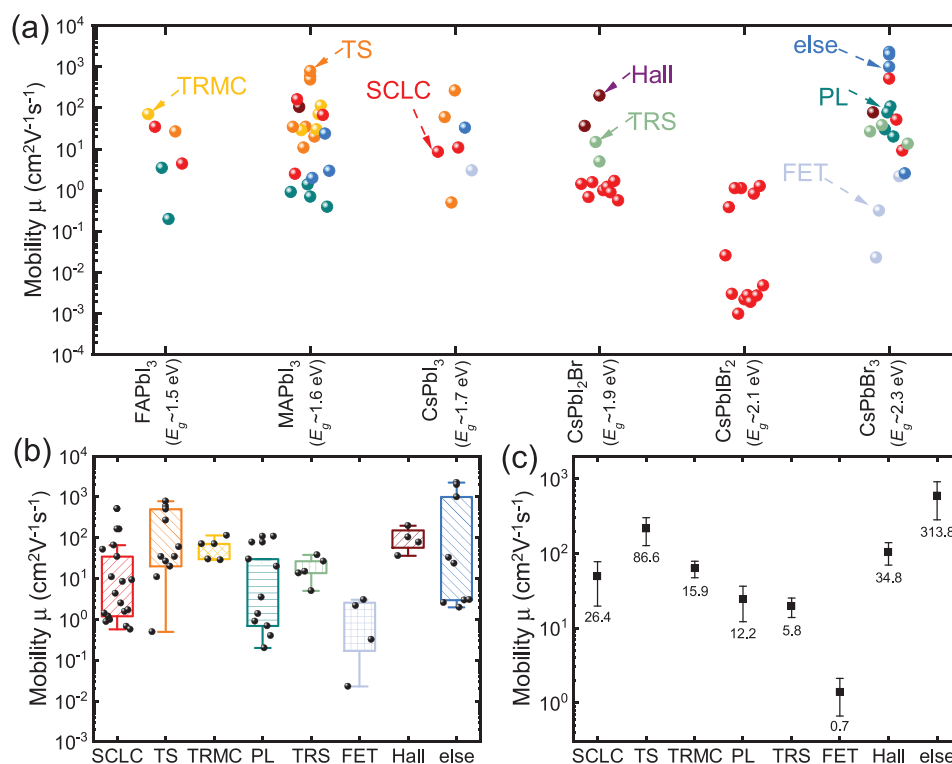


Figure 4. a) Mobility distribution of CsPbI₃,^[66,67–69] CsPbI₂Br,^[43,70–72,73] CsPbI₂Br₂,^[74] and CsPbBr₃.^[68,75,76–78] Mobility of FAPbI₃^[79] and MAPbI₃^[80,81] are also shown for comparison. The color code identifies the mobility characterization method used for each point. b) Mobility distribution of all stoichiometries shown above as a function of measurement method. c) Average mobility and standard error (the value shown in figure) of each measurement method. Please note that in the discussion of (b) and (c), we skip the mobility of CsPbI₂Br₂ as the values strongly deviated from other compositions. Hall: Hall effect measurement, SCLC: space-charge-limited current, TS: THz spectroscopy (including time-resolved THz spectroscopy and optical-pump THz-probe spectroscopy), TRMC: time-resolved microwave current, PL: photoluminescence spectroscopy (including time-resolved photoluminescence spectroscopy, photoluminescence quenching and electric field-modulated photoluminescence imaging microscopy), TRS: transient reflectance spectroscopy, FET: field-effect transistor, else (including time-of-flight, photoconductivity method, etc.).

similar carrier mobilities for all three perovskites, which has been determined to be $38 \pm 11 \text{ cm}^2 \text{ V}^{-1} \text{ s}^{-1}$, $15 \pm 1 \text{ cm}^2 \text{ V}^{-1} \text{ s}^{-1}$ and $18 \pm 2 \text{ cm}^2 \text{ V}^{-1} \text{ s}^{-1}$, respectively.^[76] According to these studies, it is generally accepted that changing the A-site cation from FA⁺, MA⁺ to Cs⁺ would not significantly affect the carrier transport. Nevertheless, more investigations are still needed, especially for the Br/I mixed anion perovskite species.

2.3. Defect Tolerance and Nonradiative Recombination

The concept of “defect tolerance”^[11] is a widely used attribute for halide perovskites, as they still possess outstanding optoelectronic properties even if they are processed from solution and form polycrystalline films with micrometer-sized grains and the associated grain boundaries. Originally, based on density functional theory (DFT) calculations, all energetically favorable intrinsic defects in perovskites were considered to be fairly shallow and in consequence were expected to have less impact on photogenerated carrier recombination, which is the so-called “shallow defect hypothesis”.^[83,84] However, further research found that at least the iodine interstitial should be a deep defect of some concern for the functionality of the device.^[85–87] Long

carrier lifetimes are one of the results of “defect tolerance. Figure 5 shows the relationship between PL lifetime τ and nonradiative open-circuit voltage loss $\Delta V_{\text{oc}}^{\text{nonrad}}$. Detailed information of the data points were shown in Table S1 (Supporting Information, Section 2). In addition, the corresponding external luminescence quantum efficiencies $Q_{\text{e}}^{\text{lum}}$ have also been calculated via the following expression

$$q(V_{\text{oc}}^{\text{rad}} - V_{\text{oc}}) = -kT \ln(Q_{\text{e}}^{\text{lum}}) \quad (2)$$

where q is the elementary charge, k is the Boltzmann constant and T is the cell temperature,^[88] while $\Delta V_{\text{oc}}^{\text{nonrad}} = V_{\text{oc}}^{\text{rad}} - V_{\text{oc}}$. The details for voltage loss calculation are introduced in Supporting Information (Section 1). We find that the CsPbBr₃ and CsPbI₂Br₂ groups exhibit shorter lifetime and higher V_{oc} loss as well as lower $Q_{\text{e}}^{\text{lum}}$. In contrast, the CsPbI_xBr_{3-x} ($2 < x < 3$) and CsPbI₃ perovskite solar cells show longer lifetime and lower voltage loss along with higher $Q_{\text{e}}^{\text{lum}}$. Giving an overview of all the presented data, there is a clear relation between τ , $\Delta V_{\text{oc}}^{\text{nonrad}}$ and $Q_{\text{e}}^{\text{lum}}$ as expected: Longer τ corresponds to lower $\Delta V_{\text{oc}}^{\text{nonrad}}$ and higher $Q_{\text{e}}^{\text{lum}}$. But it should be noted that as τ increases, the trend of $\Delta V_{\text{oc}}^{\text{nonrad}}$ reduction and $Q_{\text{e}}^{\text{lum}}$ enhancement saturates. The trend of the data in the figure is consistent with the relation

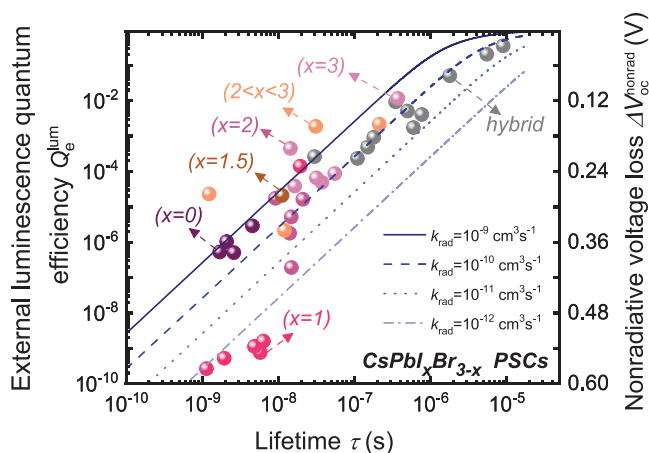


Figure 5. External photoluminescence quantum efficiency Q_e^{lum} and non-radiative voltage loss $\Delta V_{\text{oc}}^{\text{nonrad}}$ as a function of the corresponding PL lifetime τ . The lines are the calculated curves using Equation (3) for various values of k_{rad} with $p_0 = 0$, $p_a = 0$, $p_e = 0.05$, $G_{\text{ext}} = 5.3 \times 10^{21} \text{ cm}^{-3} \text{ s}^{-1}$.

between Q_e^{lum} and τ as ascribed by the following equation (see the Supporting Information of ref. [89] for a derivation)

$$Q_e^{\text{lum}} = \frac{2k_{\text{rad}}p_e\tau(p_0 + G_{\text{ext}}\tau)}{1 + k_{\text{rad}}(p_a + p_e)\tau(p_0 + 2G_{\text{ext}}\tau) + \tau\sqrt{4G_{\text{ext}}k_{\text{rad}}(p_a + p_e) + \frac{(1 + k_{\text{rad}}p_0(p_a + p_e)\tau)^2}{\tau^2}}} \quad (3)$$

with $G_{\text{ext}} = \Phi/d$, where Φ is the absorbed photon flux and d is the thickness. Furthermore, k_{rad} is the radiative recombination coefficient while p_a and p_e are the parasitic absorption and emission probability as defined and discussed in more detail in ref. [90]. Note that p_e and p_a are needed to correctly consider effects of photon recycling as discussed, e.g., in ref. [91]. Finally, Equation (3) takes doping into account by allowing to set a value for the equilibrium majority carrier concentration p_0 . Here, we assume implicitly (by naming the variable p_0) that holes are the majority carriers but Equation (3) also works for n-type doping. Furthermore, the related results from high-quality organic-inorganic hybrid perovskite solar cells have also been shown in the figure.^[89] Evidently, as for all-inorganic perovskite solar cells, there is a distinct gap with the hybrid devices in terms of lifetime τ . Even for CsPbI₃ PSC which presented the optimal $\tau = 374 \text{ ns}$,^[38] it is still over an order of magnitude shorter than the comparative optimal hybrid PSC.^[92] Such results suggest the large room for PL lifetime improvement of all-inorganic perovskite solar cells, which is the key to achieve small V_{oc} losses and high Q_e^{lum} .

Long lifetimes, high luminescence quantum efficiencies and high open-circuit voltages are directly connected as discussed in the context of Equations (2) and (3). In order to achieve long lifetimes, a material needs a low defect density and/or a slow capture coefficient of electrons and/or holes by that defect. Thus, measuring and reducing defect densities has been an important topic for essentially all photovoltaic materials. However, in particular the measurement of defects is among the most difficult challenges in the field of material and device

characterization for photovoltaics. This is at least partly due to the fact that extremely low densities of defects (relative to the total density of atoms or electrons in a material) may already have a decisive influence on device performance. There exists a multitude of methods that can—under certain conditions—allow the extraction of defect densities. However, these methods have often many caveats and can show features that may be falsely interpreted as trap densities.^[93]

For CsPbI₃-based thin films, the trap density of $8.570 \times 10^{15} \text{ cm}^{-3}$ ^[25] and $1.6 \times 10^{16} \text{ cm}^{-3}$ ^[41] were obtained by the thermally stimulated current (TSC) and transient absorption spectroscopy (TAS) methods. Space charge limited current (SCLC) measurement is the most widely used method for trap density calculation in all-inorganic perovskites. However, the results from SCLC method should be treated with caution, because there are thickness dependent detection thresholds for detecting trap densities.^[94–96] Thus, trap densities may actually be substantially lower than those measured in SCLC.

For the question of which kind of deep-level defect in all-inorganic perovskites should be responsible for nonradiative recombination, the debate still continues and no consensus has been reached. Recent research based on first-principles calculations has demonstrated that iodine interstitials (I_i) and hydrogen vacancies (V_H) are the dominant defects for nonradiative recombination in MA⁺-containing hybrid perovskite films under I-rich and I-poor conditions respectively.^[87,97] By contrast, V_H has less effect on nonradiative recombination in FA⁺-containing perovskites, which might be a reason for why FA⁺ is beneficial for achieving high performance in hybrid perovskites.^[87] With regard to all-inorganic perovskites represented by CsPbI₃, however, the existence of V_H can be ruled out since it originates from FA⁺ and MA⁺ organic cations. Nevertheless, studies on I_i for all-inorganic perovskite species have not been reported so far. In 2020, Zhang et al. have investigated deep defects Pb_i and I_{pb} in CsPbI₃. It has been revealed that the formation energy of I_{pb} is very low for I-rich conditions, while Pb_i is energetically favorable under I-poor conditions.^[86]

In order to find out how detrimental a defect is, DFT calculations can provide access to parameters such as the capture coefficients of specific defects which can then be used to compare their relative impact. Before, we discuss the results of these calculations, let us briefly explain how these quantities affect the recombination rates. The capture coefficients C_n and C_p are a property of a defect that specifies how efficiently the defect captures either electrons or holes. If one multiplies the capture coefficient with the defect density N_{def} , one obtains the inverse Shockley–Read–Hall lifetimes τ_n and τ_p for electrons and holes. These lifetimes then enter the Shockley–Read–Hall (SRH) recombination rate (R_{SRH}) and determine how many recombination events will happen per unit volume and time. The SRH recombination rate is often written as^[89]

$$R_{\text{SRH}} = \frac{(np - n_i^2)}{(n + n_1)\tau_p + (p + p_1)\tau_n} \quad (4)$$

where $n_1 = N_C \exp[(E_T - E_C)/kT]$, $p_1 = N_V \exp[(E_V - E_T)/kT]$, N_C and N_V are the effective density of states (for conduction and valence band), E_T is the trap level, E_C and E_V is the conduction

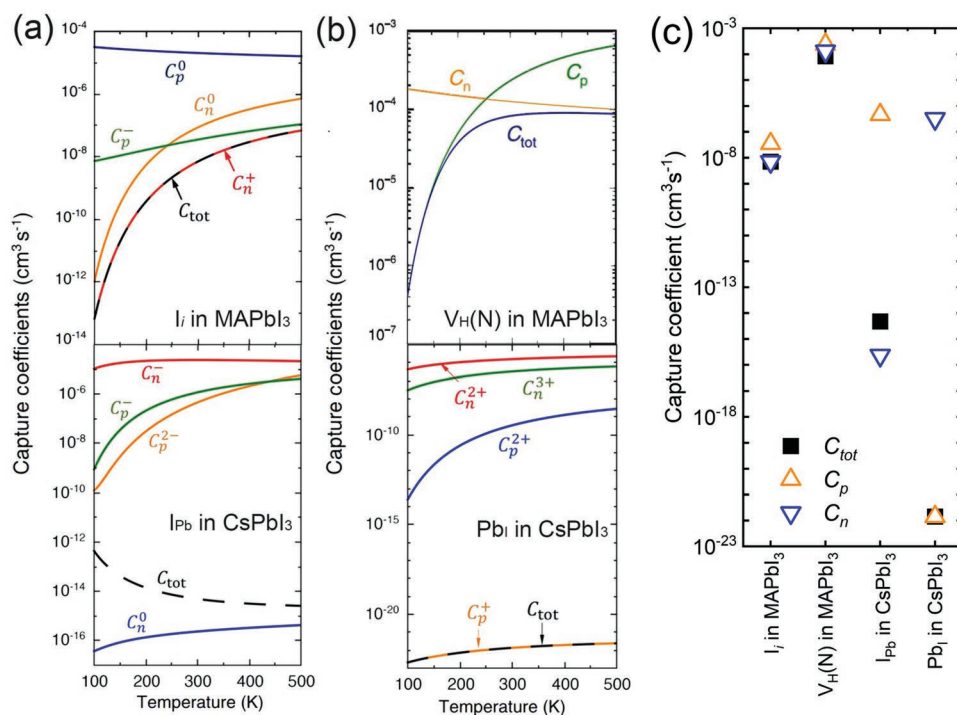


Figure 6. a) Nonradiative capture coefficient of I_i in MAPbI₃ films and I_{pb} in CsPbI₃ films as a function of temperature under I-rich condition. The curves were calculated by determining the potential energy surfaces using DFT (upper, Zhang et al., Reproduced with permission.^[97] Copyright 2020, American Physical Society; lower, Zhang et al., Reproduced with permission.^[86] Copyright 2020, American Chemical Society). b) Nonradiative capture coefficient of V_H(N) in MAPbI₃ films and Pb_i in CsPbI₃ films as a function of temperature under I-poor condition. (C_n: electron capture coefficient; C_p: hole capture coefficient.) (upper, Zhang et al., Reproduced with permission.^[87] Copyright 2021, The Authors, published by Springer Nature; lower, Zhang et al., Reproduced with permission.^[86] Copyright 2020, American Chemical Society). c) Comparison of capture coefficient under room temperature (300 K).

and valence band edges, n and p are the carrier concentration (for electrons and holes) and n_i is the intrinsic carrier concentration. Assuming that the defect levels is sufficiently deep to make thermal detrapping unlikely, we can neglect n_i and p_i , as they will then be small relative to either n or p . Thus, Equation (4) is often simplified for deep defects to^[89]

$$R_{\text{SRH}} = \frac{(np - n_i^2)}{n\tau_p + p\tau_n} \quad (5)$$

Then we use the relations of $\tau_n = 1/(C_n N_{\text{def}})$ and $\tau_p = 1/(C_p N_{\text{def}})$ ^[86,98,99] for the above equation. In case photogenerated or injected carrier concentrations are much larger than the intrinsic carrier concentration, then n_i can be ignored. In addition, considering that lead-halide perovskites typically behave as intrinsic or low-doped semiconductors, then $n = p$ can be applied. Thus we obtain^[98]

$$R_{\text{SRH}} = N_{\text{def}} \frac{C_n C_p}{C_n + C_p} n \quad (6)$$

which can be rewritten to give^[98]

$$R_{\text{SRH}} = N_{\text{def}} C_{\text{tot}} n, C_{\text{tot}} = \frac{C_n C_p}{C_n + C_p} \quad (7)$$

This implies the existence of effective carrier lifetime, defined by

$$\tau_{\text{eff}} = \frac{1}{(C_{\text{tot}} N_{\text{def}})} \quad (8)$$

Accordingly, we observe that the total capture coefficient C_{tot} is limited by the slowest capture process. In case of high C_{tot} , the defect-assisted SRH recombination rate would increase, leading to a reduction in carrier lifetime τ_{eff} . **Figure 6a,b** compare the capture coefficient curves of the deep-level defects in CsPbI₃ and MAPbI₃. The data shown in Figure 6 is based on the calculation of potential energy surfaces and configuration coordinate diagrams of the different states involved in the recombination event using DFT. The DFT was performed using the Heyd–Scuseria–Ernzerhof (HSE) hybrid functional including spin–orbit coupling.^[86,87,97,100] Zhang et al. report I_i to be the dominant defect in MAPbI₃ films having a low formation energy especially under I-rich condition. As shown in Figure 6a, the process of electron capture by I_i⁺ (i.e., C_n⁺) exhibits the slowest capture coefficient of $0.7 \times 10^{-8} \text{ cm}^3 \text{ s}^{-1}$ at room temperature, indicating the same order of magnitude for C_{tot}.^[97] As for CsPbI₃, only I_{pb} deep defects have been shown to have low formation energies under I-rich condition so far. In Figure 6a, the electron capture by I_{pb}⁰ (i.e., C_n⁰) is the slowest process, which limits the total capture coefficient on the order of $10^{-14} \text{ cm}^3 \text{ s}^{-1}$ at room temperature.^[86] On the other hand,

the $V_{\text{H}}(\text{N})$ in MAPbI_3 possess low formation energy (0.72 eV) under I-poor condition and its C_{tot} curve is affected by both C_{n} and C_{p} . As shown in Figure 6b, the C_{tot} depends on C_{n} at room temperature, suggesting the C_{tot} of $0.8 \times 10^{-4} \text{ cm}^3 \text{ s}^{-1}$ for $V_{\text{H}}(\text{N})$ under this circumstance.^[87] With regard to Pb_i deep defects in CsPbI_3 under I-poor condition (Figure 6b), the C_{tot} is limited by the hole capture coefficient of Pb_i^+ (i.e., C_{p}^+), which is only $10^{-22} \text{ cm}^3 \text{ s}^{-1}$.^[86] Evidently, though Pb_i and I_pb deep defects in CsPbI_3 possess low formation energy, both of them exhibit extremely slow C_{tot} , which are much slower than the dominant deep defects (I_i and $V_{\text{H}}(\text{N})$) in MAPbI_3 . Zhang et al. have attributed the low rates to the presence of strong anharmonicity in the potential energy surfaces that describe the charge-state transitions.^[86] However, the dominant defects for nonradiative recombination in CsPbI_3 have not been identified yet. Additionally, it is observed that the capture coefficient for electrons is quite different from that for holes in perovskites, which can be better illustrated in Figure 6c. This result suggests a new route for the improvement of defect tolerance in perovskites. As demonstrated in ref. [101], when the capture coefficient for holes is higher than that for electrons, the recombination could be further reduced by slowing down the electron capture through reducing the electron concentration and increasing the hole concentration,^[101] which is feasible during the preparation process. Moreover, as shown in Figure 6c, the C_{n} of I_pb is 9 orders of magnitude lower than the related C_{p} in CsPbI_3 , as well as the C_{p} of Pb_i is 14 orders of magnitude lower than the related C_{n} . Such difference is much larger than that of I_i and $V_{\text{H}}(\text{N})$ in MAPbI_3 , which may be beneficial for the optoelectronic performance of CsPbI_3 -based devices.

Apart from CsPbI_3 , the formation energy and charge transition level of defects in CsPbBr_3 have been investigated by DFT calculation as well. Reported by Kang and Wang, most of the defects in CsPbBr_3 films are shallow, while the two antisite defects Pb_Br , Br_Pb , and the lead interstitial (Pb_i) can introduce deep transition levels.^[83] Fortunately, these three deep-level defects have large formation energies which has been attributed to the lack of bonding–antibonding interaction between the conduction bands and valence bands.^[83] In addition, Swift and Lyons have demonstrated that the hydrogen interstitial (H_i) and bromine interstitials (Br_i) are deep-level defects in CsPbBr_3 as well, and show relatively low formation energy under Pb-rich

and Br-rich condition respectively.^[85] However, their effect on carrier capture process is still unclear.

With regard to mixed halide all-inorganic perovskites, i.e., CsPbIBr_2 , CsPbI_2Br , and etc., it is believed that phase segregation spontaneously happens when mixing different halogens because of the bonding energy difference between Pb–Br and Pb–I bonds.^[102] Unfortunately, few theoretical studies focusing on deep-level defects in mixed halide perovskites have been reported so far and therefore more efforts on this topic are strongly needed.

3. Solar Cells

3.1. Structure

At present, the typical layer stack of all-inorganic perovskite solar cells is identical to that of many organic–inorganic hybrid perovskite solar cells, which commonly includes FTO (or ITO) glass substrate, perovskite absorber layer, HTL, ETL and electrode, as illustrated in Figure 7. To be specific, it can be classified into several types, i) mesoscopic; ii) planar regular (n–i–p) and iii) planar inverted (p–i–n) structures. Many highly efficient CsPbBr_3 and CsPbIBr_2 perovskite solar cells with wide bandgaps have adopted carbon-based HTL-free structure,^[103] which is partly because of the lack of highly efficient HTLs for them. For all-inorganic perovskite solar cells, fewer works with planar inverted structure have been reported, which results from the fact that the conventional organic transport layer materials (e.g., poly(triaryl amine) (PTAA) and poly(3,4-ethylenedioxythiophene) polystyrene sulfonate (PEDOT:PSS)) cannot withstand the typical temperatures of 200 °C to 250 °C used for annealing of inorganic perovskites. In this case, inorganic NiO_x film is the most commonly used HTL for planar inverted devices. Alex K. Y. Jen's group has made substantial contributions to the field of inverted all-inorganic perovskites. The best efficiencies obtained in this structure was 16.10% (certified: 15.6%) using the layer stack $\text{ITO}/\text{NiO}_x/\text{CsPbI}_x\text{Br}_{3-x}/\text{6TIC-4F}/\text{ZnO}/\text{C}_{60}/\text{Ag}$.^[104] High PCE up to 20.37% has been reported for all-inorganic PSC with planar regular structure,^[25] as well as 17.16% PCE for that with mesoscopic structure,^[47] suggesting the large room for planar inverted all-inorganic perovskite solar cells improvement. Thus, more

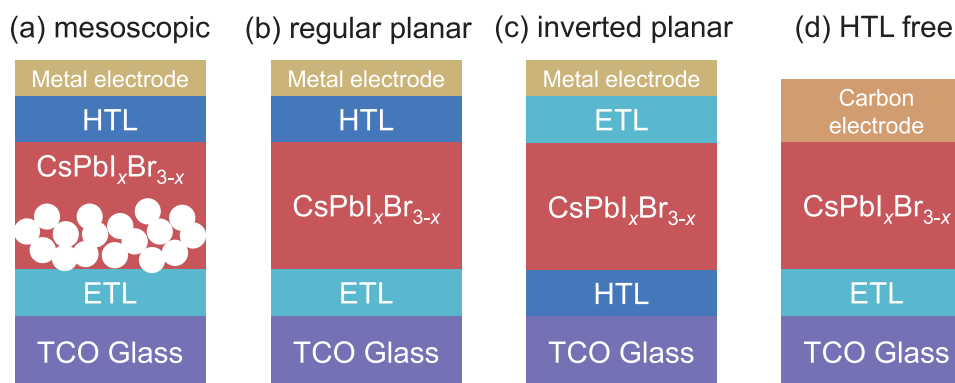


Figure 7. Typical device diagrams of $\text{CsPbI}_x\text{Br}_{3-x}$ ($0 \leq x \leq 3$) perovskite solar cells. a) mesoscopic structure, b) regular planar (n–i–p) structure, c) inverted planar (p–i–n) structure, d) carbon-based HTL-free structure which widely adopted for CsPbBr_3 and CsPbIBr_2 perovskite solar cells.

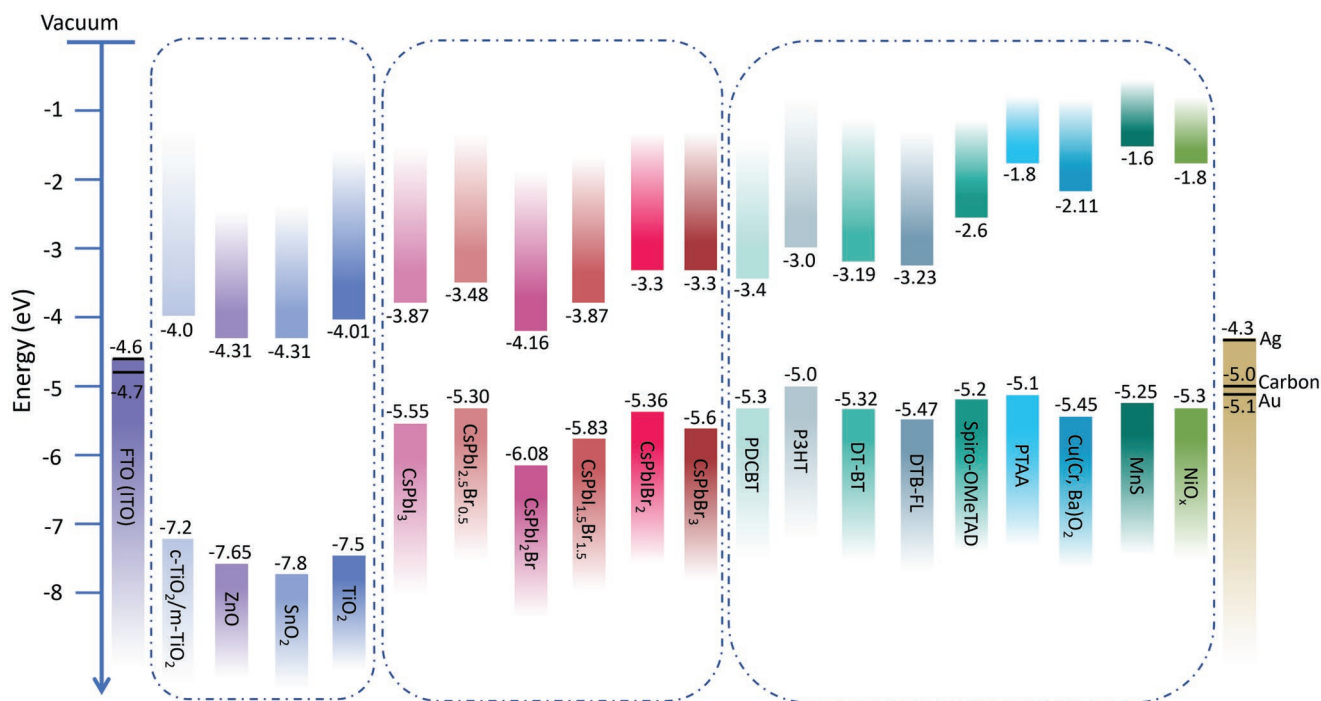


Figure 8. Energy levels of recently reported $\text{CsPbI}_x\text{Br}_{3-x}$ ($0 \leq x \leq 3$) films and highly efficient transport layers according to refs. [20,40,41,49,56,60,61,105–108], which were mainly obtained from absorption spectra and photoelectron spectroscopy. Note that the valence and conduction band levels as well as the work function may vary depending on the exact stoichiometry but also on the mode of preparation and surface treatments.

efforts on inverted all-inorganic perovskite solar cells are needed, as well as on highly efficient inorganic HTLs exploration.

Figure 8 illustrates energy levels of typical transport layer materials for highly efficient all-inorganic perovskite solar cells, along with that of perovskite absorber layers. For ETLs, TiO_2 , SnO_2 , ZnO and $\text{c-TiO}_2/\text{m-TiO}_2$ are most commonly used for highly efficient perovskite solar cells, which are inorganic materials and have been fully investigated and optimized for hybrid perovskite solar cells. For perovskite solar cells with regular or mesoscopic structure, HTLs would not be affected by the high-temperature process, leading to a large variety of materials to choose. Apart from the most frequently used 2,2,7,7-tetrakis(*N,N*-dimethoxy-phenylamine)-9,9-spirobifluorene (spiro-MeOTAD) films, other organic materials, such as poly[bis-(4-phenyl)-(2,4,6-trimethylphenyl)-amine] (PTAA), poly(3-hexylthiophen-2,5-diyl) (P3HT) and poly[5,5'-bis(2-butyloctyl)-(2,2'-bithiophene)-4,4'-dicarboxylate-*alt*-5,5'-2,2'-bithiophene] (PDCBT), have also been reported for high-efficient all-inorganic perovskite solar cells. Niu et al. have explored some D–A– π –A–D-type hole-transport materials which have advantages of dopant-free, low-cost and stable, and applied for $\text{CsPbI}_{2.5}\text{Br}_{0.5}$ perovskite solar cells, achieving a PCE of 17.0%.^[105] However, the conventional hole-transport materials are not suitable for CsPbBr_3 and CsPbI_2Br perovskite solar cells. In consequence, HTL-free carbon electrode structure has been developed and new-type of inorganic transport layer materials have been explored basing on such structure. Tang's group have successively developed $\text{Cu}(\text{Cr}, \text{Ba})\text{O}_2$ nanocrystals (NCs),^[60] $\text{CuInS}_2/\text{ZnS}$ quantum dots (QDs)^[31] and brominated graphene oxide (Br-GO)^[109] materials to act as HTLs for CsPbBr_3 perovskite solar cells.

3.2. Device Fabrication

Most all-inorganic perovskite solar cells reported in the literature so far have been prepared using solution processing methods such as spin-coating, spray coating and blade coating. So far, most highly efficient all-inorganic perovskite solar cells have been prepared by spin-coating, including the devices with a PCE over 20%. Spray coating and blade coating are in general more suitable to prepare devices that exceed the areas $<1 \text{ cm}^2$ typically used in research. Up to now, larger-area all-inorganic perovskite solar cells with PCE of 13.82% (112 cm^2 , regular $\text{CsPbI}_{3-x}\text{Br}_x$ ($2 < x < 3$) solar cell)^[110] and 10.73% (8 cm^2 , regular CsPbI_3 solar cell)^[111] have been reported by using spray coating and blade coating, respectively. A challenge for depositing multinary semiconductors on larger areas can be lateral inhomogeneities in thicknesses but also in composition, bandgap or other film qualities such as stress or strain or the density of recombination active defects. Specific research on upscaling and avoiding of spatial inhomogeneities in all-inorganic perovskite solar cells is so far still scarce. Early examples are the demonstration of Mai and co-workers who showed that increasing the transport layer thickness can relieve the leakage loss to some extent leading to a PCE of 12.19% for a 10.92 cm^2 area achieved (inverted CsPbI_2Br solar cell), however, still by spin-coating.^[71]

Another challenge for the upscaling and technological maturity of solution processing is to find alternatives for the toxic solvents that are used in the large majority of academic research efforts on lead-halide perovskites. While there have been sufficient investigations on “green” solvents for hybrid perovskites in general,^[112] we just find very few investigations in the context of all inorganic perovskites and the performance is still not as

good as the traditional solvents.^[113] Vapor deposition methods such as evaporation have advantages with regard to the absence of any solvents but have the disadvantage of requiring costly vacuum equipment as well as fairly long deposition times as compared to solution processing. Until now, the champion efficiency of all-inorganic perovskite solar cell prepared by vapor deposition is 13% (0.051 cm², regular CsPbI₂Br solar cell).^[114] Furthermore, a small amount of studies on large-area devices were reported, among which the highest PCE of 9.4% (1 cm², regular CsPbI₂Br solar cell) was achieved by single source evaporation.^[115]

3.3. Stability

Though all-inorganic perovskites are facing phase transition issue as mentioned above, however, they still possess satisfying stability, particularly the thermal stability. It is known that organic-inorganic hybrid perovskites cannot endure high-temperature treatment because of the existence of MA⁺ and FA⁺ organic cation. It has been reported that MAPbI₃ have the risk of decomposition at temperatures of 85 °C,^[118] while the decomposition temperature for FAPbI₃ is approximately 150 °C.^[119] In general, 250–350 °C is required for inorganic materials preparation via regular thermal processes and satisfyingly, Cs⁺-based all-inorganic perovskites would not occur decomposition issue under this circumstance. Such favorable thermal stability could not only improve the durability of the whole device, but also be able to adapt to more high-temperature technologies. This is especially useful for constructing devices with complex

structures (e.g., tandem devices). Many reviews outlining the status, mechanism and optimization process of stability for all-inorganic perovskite devices have been reported.^[119,120] Here we just list some typical works to reveal the status of stability for all-inorganic perovskite solar cells with different *x* values. Required by the International Electrotechnical Commission, the assessment criteria for photovoltaic stability should meet that both moisture (80% relative humidity) and heat (80 °C) stabilities are more than 2000 h. Compared to the organic-inorganic hybrid perovskites, the all-inorganic species are apparently closer to these requirements. Chen et al. have developed a PbI₂·*N*-methyl-2-pyrrolidone (NMP)-assisted growth method for high-quality α -CsPbI₃ films and used 18-crown-6 ether to suppress water invasion and passivate defects, and thus achieved stable α -CsPbI₃ perovskite solar cells, which readily maintained \approx 91% of the initial PCE for more than 1000 h (85 °C, N₂) and even \approx 90% for up to 2000 h (25 °C, 20% relative humidity) without encapsulation (Figure 9a).^[111] Furthermore, a stability performance that retained \approx 95% of the original value for over 500 h (operating conditions, 60% relative humidity) with encapsulation has also been achieved.^[111] As shown in Figure 9b, Han et al. have reported CaCl₂-doped CsPbI₂Br devices which maintains \approx 90% of its initial efficiency after 1080 h when stored and tested in air (\approx 25% relative humidity).^[116] Zhu et al. fabricated unencapsulated CsPbI₂Br₂ devices maintaining \approx 90% of the initial PCE after storing for 60 days (1440 h) at 25 °C and 45% relative humidity (Figure 9c), as well as \approx 97% PCE after storing for 7 days (168 h) at 85 °C with water content below 1 ppm.^[52] With regard to CsPbBr₃ perovskite solar cells, as they are usually fabricated using carbon electrodes rather than Au or Ag electrodes

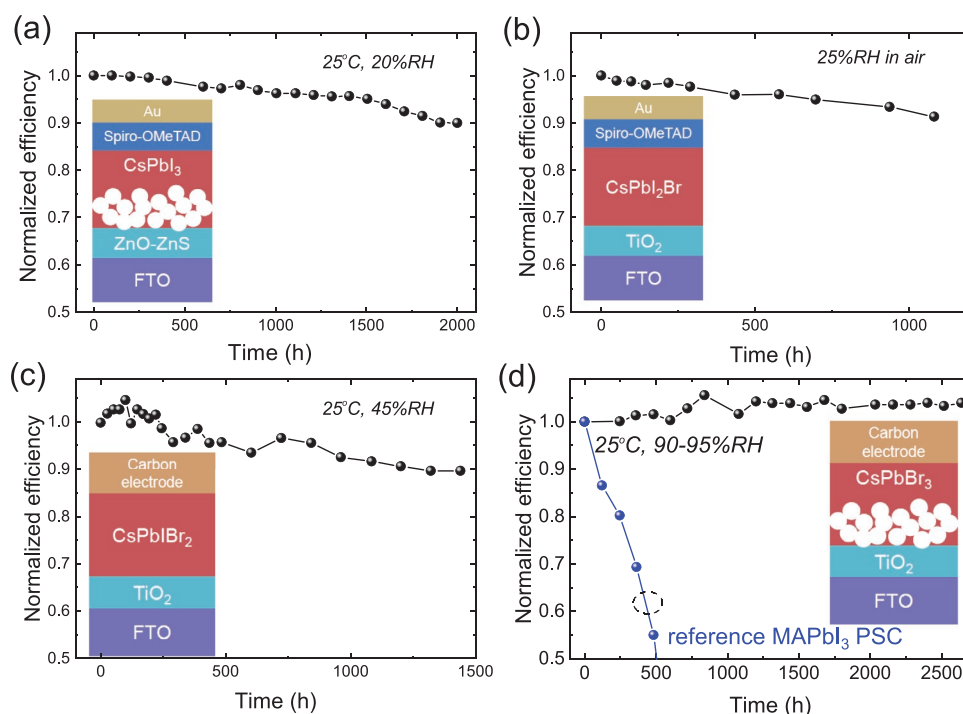


Figure 9. Storage stability measurement results of the representative unencapsulated all-inorganic perovskite solar cells. All figures are replotted based on the data in the following publications: a) CsPbI₃ PSC reported by Chen et al.,^[111] b) CsPbI₂Br PSC reported by Han et al.,^[116] c) CsPbI₂Br₂ PSC reported by Zhu et al.,^[52] d) CsPbBr₃ and the reference MAPbI₃ perovskite solar cells reported by Liang et al.^[117]

and getting rid of organic HTLs, which is beneficial to avoid moisture absorption and thermal decomposition of organic HTLs and oxidation of metal electrodes, CsPbBr₃ devices exhibit superior stability among all-inorganic perovskites. Early in 2016, Liang et al. have investigated CsPbBr₃ device with FTO/c-TiO₂/m-TiO₂/CsPbBr₃/carbon structure. The unencapsulated PSC showed none degradation after storing for 3 months (2640 h) at 25 °C and 90–95% relative humidity, while the reference MAPbI₃ devices degraded to ≈10% of its initial value after storing for ≈720 h (Figure 9d).^[117] Furthermore, they have also demonstrated that the use of organic spiro-MeOTAD HTL would fasten the degradation of device performance. Furthermore, in high-temperature and high-humidity conditions (100 °C, 90–95% relative humidity), the unencapsulated CsPbBr₃ PSC still presented no degradation after 840 h storage, while the MAPbI₃ device with the same structure could only remain stable in the initial 20 h.^[117] These results suggest that apart from considering film quality, grain boundary and phase stability, substitution of organic HTLs is a promising strategy for PSC stability improvement.

3.4. Performance

In this section, we review the key photovoltaic performance indicators (i.e., J_{sc} , V_{oc} , FF, and η) of high-quality CsPbI_xBr_{3-x}-based perovskite solar cells and mainly focus on the comparison between the experimental values and the corresponding

SQ limits. Also, we discuss surface and interface passivation approaches for the devices. Detailed performance indicators are shown in **Figure 10**, **Figure 11** and **Tables 1–5** while the correspondence between data points and authors being found in Figure S4–S8 in Supporting Information (Section 3). We mainly focus on the perovskite solar cells with the best PCEs in their own group. As shown in Tables 1–5, it can be seen that the bandgaps of materials or devices as well as the accurate calculation process have not been performed in many publications, leading to the difficulty for sensible loss analysis and straightforward performance comparison for the all-inorganic perovskite solar cells. Fortunately, the dataset of external quantum efficiency has been provided in the vast majority of publications, making it pretty possible for the calculation of E_g^{ip} . Thus, we list the values of E_g^{ip} calculated from the corresponding EQE dataset in the tables, as well as the ratio of V_{oc}/V_{oc}^{SQ} , J_{sc}/J_{sc}^{SQ} , FF/FF^{SQ}, η/η^{SQ} basing on the calculated E_g^{ip} . The detailed calculation progress of E_g^{ip} energies can be found in the Supporting Information (Section 1.1 and 1.2) while the corresponding figures are shown in Supporting Information (Appendix). For a small number of publications, the EQE dataset were lacking, which results in the unavailable E_g^{ip} values (marked as “N/A” in the table). In addition, it is observed that though the calculated E_g^{ip} values are close to the reported bandgap E_g^{rep} for most publications; somewhat large deviations do exist in some publications. Thus, we discuss about the deviation for these samples and demonstrate the rationality and reliability of the calculated E_g^{ip} values in the Supporting Information (Section 4). The

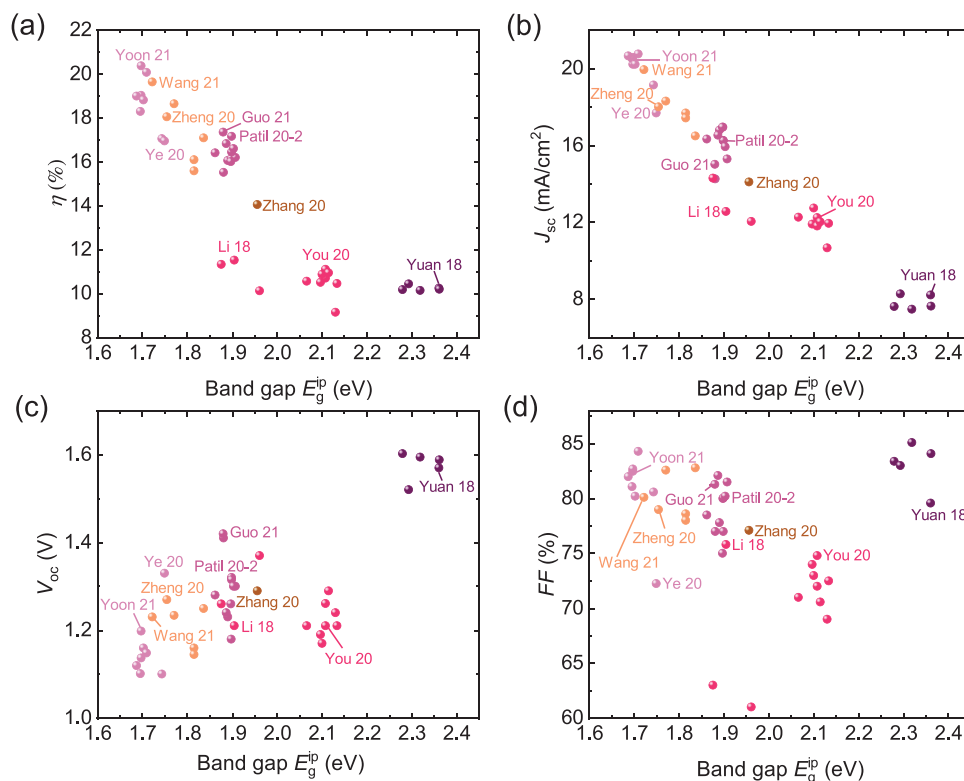


Figure 10. a) Efficiency; b) short-circuit current density; c) open-circuit voltage and d) fill factor along with E_g^{ip} for the recently reported high-quality perovskite solar cells based on CsPbI_xBr_{3-x} ($0 \leq x \leq 3$). The color of the datapoints represents the stoichiometric ratio of iodine (x) for the perovskite materials (plum: $x = 3$, orange: $2 < x < 3$, violet: $x = 2$, sienna: $x = 1.5$, deep-pink: $x = 1$, purple: $x = 0$).

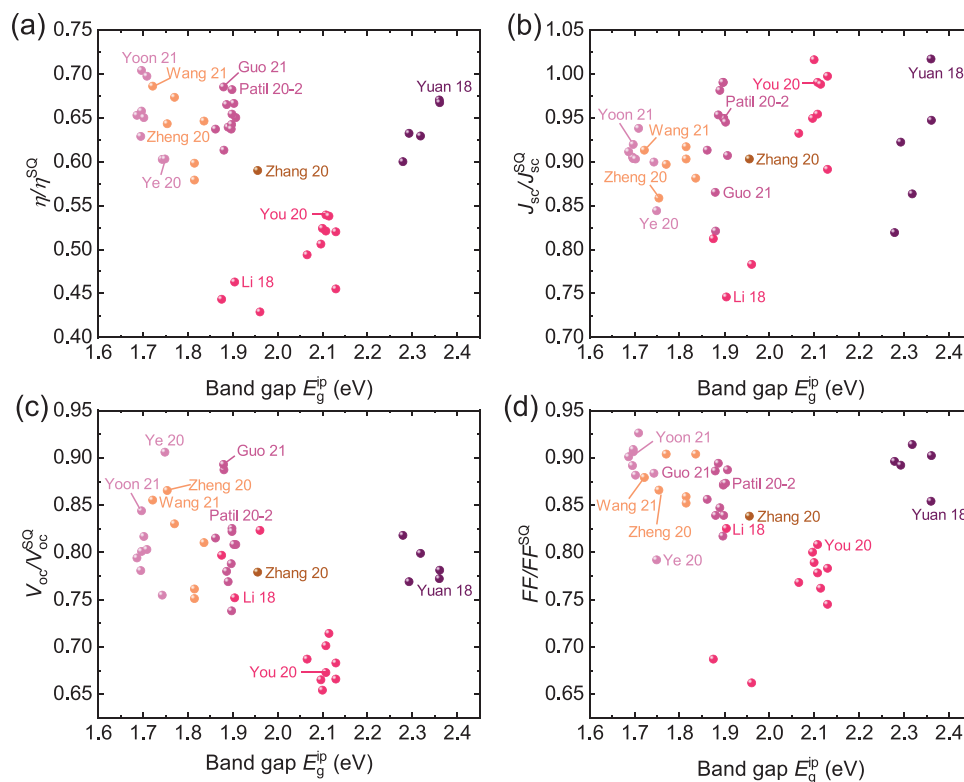


Figure 11. a–d) The ratio of η/η^{SQ} (a); $J_{\text{sc}}/J_{\text{sc}}^{\text{SQ}}$ (b); $V_{\text{oc}}/V_{\text{oc}}^{\text{SQ}}$ (c), and FF/FF^{SQ} (d) along with E_{g}^{ip} for the recently reported high-quality perovskite solar cells based on $\text{CsPbI}_x\text{Br}_{3-x}$ ($0 \leq x \leq 3$). The color of the datapoints represents the stoichiometric ratio of iodine (x) for the perovskite materials (plum: $x = 3$, orange: $2 < x < 3$, violet: $x = 2$, sienna: $x = 1.5$, deep-pink: $x = 1$, purple: $x = 0$).

reasons for the deviation could be attributed to the followings, i) the effect of functional layers such as transport layers and interfacial layers. Absorbance by the functional layers broadens the absorption range, which would have effect on the bandgap of the devices in the case of constant perovskite-layer bandgap. ii) the effect of subsequent processes. The preparation of transport layers, interfacial layers and electrodes via chemical and heating processes would affect the perovskite layers which cannot be reflected by the conventional Tauc method. iii) calculation errors. The stated E_{g} values using Tauc method is determined by a fit of the linear region of $(\alpha h\nu)^2$ versus $h\nu$ and extrapolation to the x -axis, which is more error prone as compared to the calculation of E_{g}^{ip} values. Hence, we conclude that it would be more sensible to use the E_{g}^{ip} values for the performance loss analysis in these cases.

3.4.1. Performance Variations with Stoichiometry

Figure 10 and Figure 11 summarize the distribution of the parameters efficiency (a); short-circuit current density (b); open-circuit voltage (c), and fill factor (d) as a function of E_{g}^{ip} . In Figure 10, we show the absolute values of the four parameters, while in Figure 11 we normalize each parameter to the corresponding value in the SQ model. In Figure 10 the trends for efficiency, J_{sc} and V_{oc} are dominated by the trends inherent to the SQ model. Efficiencies decrease strongly with bandgap, because the loss in J_{sc} for higher bandgaps overcompensates

any gains in V_{oc} . The only part of the stoichiometry range that severely underperforms relative to the rest is $\text{CsPbI}_1\text{Br}_2$. To compensate for the SQ-inherent trends with bandgap, the normalized values are shown in Figure 11. Here, the most noteworthy aspect is the anticorrelation between the normalized V_{oc} (Figure 11c) and the normalized J_{sc} (Figure 11b). The normalized V_{oc} decreases and the normalized J_{sc} increases with bandgap. Thus, the normalization inverses the trends seen in Figure 10.

Because of the significant effect of the stoichiometry of the perovskite characterized by the x value on the bandgap, stability and photovoltaic performance of the devices, we discuss the present high-quality all-inorganic perovskite solar cells in detail as a function of the x value. As shown in Figure 11a, the champion η of present all-inorganic perovskite solar cells approaches 70% of the SQ limit. Nevertheless, only a few high-quality CsPbI_3 -based have approached such a ratio. As for the majority of devices, the ratio of η/η^{SQ} is around 60–70% ($x \geq 2$ and $x = 0$), while the ratio is even lower than 60% when $x = 1$ or 1.5. Furthermore, most of the samples exhibit high-level J_{sc} performance, with $J_{\text{sc}}/J_{\text{sc}}^{\text{SQ}}$ ratio achieving to 90% or even higher (Figure 11b). Some devices show ultra-high values close to or above 1 which seem unreasonable and will be discussed later. As shown in Figure 11d, the variation of FF/FF^{SQ} ratio with bandgap is similar to that of η/η^{SQ} , with the majority of data points being in the 80–95% range. In Figure 11c, the $V_{\text{oc}}/V_{\text{oc}}^{\text{SQ}}$ ratios of most devices show relatively low values at around 80% or even lower, which is the main

Table 1. Performance indicators of reported high-quality CsPbI₃ ($x = 3$) solar cells. Abbreviations: MACl: methylammonium chloride, SDMS: sequential dripping of a methylammonium chloride solution, OAI: octylammonium iodide, DMAI: dimethylammonium iodide, PTACl: phenyltrimethylammonium chloride, CHI: choline iodide, PTABr: phenyltrimethylammonium chloride bromide, PEA: phenylethylammonium.

Structure (key technology)	$E_{\text{g}}^{\text{rep}}$ [eV]; E_{g}^{ip} [eV]	V_{oc} [V]; $V_{\text{oc}}/V_{\text{oc}}^{\text{SQ}}$	J_{sc} [mA cm ⁻²]; $J_{\text{sc}}/J_{\text{sc}}^{\text{SQ}}$	FF [%]; FF/FF ^{SQ}	η [%]; η/η^{SQ}	Ref.
FTO/TiO ₂ /α-CsPbI ₃ :PTABr/spiro-OMeTAD/Ag (PTABr surface post-passivation)	N/A 1.743	1.10; 75.4%	19.15; 89.9%	80.6; 88.4%	17.06; 60.3%	Yong Wang 2018 ^[36]
FTO/c-TiO ₂ /β-CsPbI ₃ :CHI/spiro-OMeTAD/Ag (DMAI volatile additive and CHI surface passivation)	1.68; 1.695	1.101; 78.1%	20.525; 90.5%	81.1; 89.1%	18.3; 62.9%	Yong Wang 2019 (certified) ^[26]
FTO/c-TiO ₂ /β-CsPbI ₃ :PTACl/spiro-OMeTAD/Ag (DMAI volatile additive and PTACl surface passivation)	N/A; 1.698	1.137; 80.1%	20.23; 90.4%	82.7; 90.9%	19.03; 65.7%	Yong Wang 2019-2 ^[37]
ITO/SnO ₂ /LiF/γ-CsPbI ₃ :PEA/spiro-OMeTAD/Au (PEA and Pb(OAc) ₂ induced 3D/2D structure)	1.71; 1.749	1.33; 90.6%	17.7; 84.4%	72.25; 79.2%	16.95; 60.3%	Qiufeng Ye 2020 ^[38]
FTO/SnO ₂ /CsPbI ₃ :Zn(C ₆ F ₅) ₂ /CsPbI ₃ /spiro-OMeTAD/Au (Zn(C ₆ F ₅) ₂ additive and blade-coating)	1.68; 1.687	1.12; 79.4%	20.67; 91.1%	81.98; 90.1%	19.00; 65.3%	Xiaoming Chang 2020 ^[39]
FTO/TiO ₂ /CsPbI ₃ /2D-CsPbI ₃ /spiro-OMeTAD/MoO ₃ /Ag (2D capping layer on 3D perovskite)	1.69; 1.702	1.16; 81.7%	20.22; 90.3%	80.23; 88.1%	18.82; 65.0%	Tiantian Liu 2021 ^[40]
FTO/TiO ₂ /CsPbI ₃ /spiro-OMeTAD/Au (Urea-ammonium thiocyanate additive)	1.68; 1.709	1.148; 80.3%	20.76; 93.8%	84.3; 92.6%	20.08; 69.7%	Bingcheng Yu 2021 ^[41]
FTO/c-TiO ₂ /β-CsPbI ₃ :45MACl/spiro-OMeTAD/Au (SDMS method and OAI surface passivation)	N/A; 1.697	1.198; 84.4%	20.59; 92.0%	82.5; 90.6%	20.37; 70.4%	So Me Yoon 2021 ^[25]

factor limiting the η/η^{SQ} value enhancement for most of all-inorganic perovskite solar cells.

High-quality CsPbI₃-based ($x = 3$) perovskite solar cells and CsPbI_xBr_{3-x}-based ($2 < x < 3$) perovskite solar cells are the most attractive species in the field of all-inorganic perovskite solar cells and they exhibit similar performances. The η/η^{SQ} values of most of these devices are between 60% and 70%. The ratios of $J_{\text{sc}}/J_{\text{sc}}^{\text{SQ}}$ and FF/FF^{SQ} are close to or even beyond 90% for some devices. In contrast, the $V_{\text{oc}}/V_{\text{oc}}^{\text{SQ}}$ ratios of most devices show relatively low values at around 80%. Yoon et al. have reported a recorded efficiency of 20.37% with which η/η^{SQ} value reaching 70.4%.^[25] This is the only one with η/η^{SQ} ratio exceeding 70% so far. In addition, Yu et al. have obtained a device with excellent $J_{\text{sc}}/J_{\text{sc}}^{\text{SQ}}$ and FF/FF^{SQ} of 93.8% and 92.6% respectively.^[41] Wang et al. have investigated CsPbI₃ perovskite solar cells and mainly focus on surface passivation and has achieved a certified efficiency of 18.3%.^[26,36,121] Ye et al. have exploited 2D/3D mixed dimensional CsPbI₃ perovskite solar cells and obtained an ultrahigh $V_{\text{oc}}/V_{\text{oc}}^{\text{SQ}}$ value of 90.6%, which is the only device with the value beyond 90%.^[38] The CsPbI_xBr_{3-x} ($2 < x < 3$) perovskite solar cells from Zheng et al. also based on the 2D/3D mixed dimensional structure, achieving an excellent $V_{\text{oc}}/V_{\text{oc}}^{\text{SQ}}$ ratio of 86.5% as well.^[122] Recently, Wang et al.

(2021) have reported an β-CsPbI_{2.85}Br_{0.149}Cl_{0.001}-based device with attractive performance of $V_{\text{oc}}/V_{\text{oc}}^{\text{SQ}}$, $J_{\text{sc}}/J_{\text{sc}}^{\text{SQ}}$, η/η^{SQ} and η reaching 85.5%, 91.3%, 68.6% and 19.65%, respectively.^[28] The η/η^{SQ} and $V_{\text{oc}}/V_{\text{oc}}^{\text{SQ}}$ values of high-quality CsPbI₂Br-based perovskite solar cells are around 66% and 80% respectively, while the ratio of $J_{\text{sc}}/J_{\text{sc}}^{\text{SQ}}$ exhibits higher values up to ≈96%. However, the FF/FF^{SQ} values are relatively lowered, the maximum value of which is less than 90%. Guo et al. have reported CsPbI₂Br perovskite solar cells with a champion PCE of 17.36%^[29] in this group, achieving 68.5% of η/η^{SQ} and 89.3% of $V_{\text{oc}}/V_{\text{oc}}^{\text{SQ}}$ ratios simultaneously. Patil et al. have fabricated Rb-doped CsPbI₂Br perovskite solar cells with a PCE of 17.16%,^[47] acquiring 68.2% of η/η^{SQ} . Moreover, CsPbI₂Br₂ and CsPbI_{1.5}Br_{1.5} perovskite solar cells were put together for comparison due to their similar E_{g}^{ip} energies. This group of perovskite solar cells present much larger room for performance improvement by comparison with the corresponding values in the SQ model, for which the ratios of η/η^{SQ} , $V_{\text{oc}}/V_{\text{oc}}^{\text{SQ}}$ and FF/FF^{SQ} just come out to around ≈40-60%, ≈75% and ≈78% respectively. Zhang et al. have demonstrated a high PCE of 14.05% for CsPbI_{1.5}Br_{1.5}-based device with 59.0% of η/η^{SQ} ratio.^[106] For the CsPbI₂Br₂ devices with E_{g}^{ip} close to the intrinsic value (≈2.1eV), they usually show good $J_{\text{sc}}/J_{\text{sc}}^{\text{SQ}}$ and η/η^{SQ} values. You et al. have reported a CsPbI₂Br₂

Table 2. Performance indicators of reported high-quality CsPbI_xBr_{3-x} (2 < x < 3) solar cells. Abbreviations: TL: transport layer, MAAC: methylammonium acetate, FAOAc: formamidinium acetate.

Structure (key technology)	E_g^{exp} [eV]; E_g^{ip} (eV)	V_{oc} [V]; $V_{\text{oc}}/V_{\text{oc}}^{\text{SQ}}$	J_{sc} [mA cm ⁻²]; $J_{\text{sc}}/J_{\text{sc}}^{\text{SQ}}$	FF [%]; FF/FF ^{SQ}	η [%]; η/η^{SQ}	Ref.
ITO/SnO ₂ /CsPb(I _{0.85} Br _{0.15}) ₃ /spiro-OMeTAD/Au (solvent-controlled crystal growth)	N/A; N/A	1.22; N/A	17.3; N/A	77.5; N/A	16.14; N/A	Pengyang Wang 2018 ^[124]
ITO/SnO ₂ /LiF/CsPbI _x Br _{3-x} /spiro-OMeTAD/Au (LiF interface layer and PbCl additive)	1.77; 1.771	1.234; 83.0%	18.3; 89.7%	82.58; 90.4%	18.64; 67.3%	Qiufeng Ye 2019 ^[125]
FTO/c-SnO ₂ /CsPb(I _{0.75} Br _{0.25}) ₃ :FAOAc/spiro-OMeTAD/Au (intermediate-phase engineering with volatile salts)	1.86; 1.859	1.34; 85.3%	15.9 88.9%	79.6; 86.8%	17.0; 66.0%	Jiahuan Zhang 2020 ^[126]
ITO/SnO ₂ /SIM-CsPbI _x Br _{3-x} /spiro-OMeTAD/Au (spontaneous interfacial manipulation 2D/3D top interface)	≈1.75; 1.754	1.27; 86.5%	18.01; 85.8%	0.79; 86.6%	18.06; 64.3%	Yifan Zheng 2020 ^[122]
FTO/SnO ₂ /CsPbI _{2.5} Br _{0.5} /spiro-OMeTAD/MoO ₃ /Ag (MAAC solvent)	N/A; N/A	1.3; N/A	17.67; N/A	74.18; N/A	17.10; N/A	Xiaojuan Wang 2020 ^[127]
ITO/SnO ₂ /ZnO/CsPbI _{2.5} Br _{0.5} /spiro-OMeTAD/Ag (Composition Engineering with excess PbI ₂)	1.82; 1.836	1.25; 81.0%	16.5; 88.1%	82.8; 90.4%	17.1; 64.6%	Jingjing Tian 2020 ^[107]
ITO/SnO ₂ /CsPbI _{2.5} Br _{0.5} /HTM/DTB-FL/Ag (HTL design)	N/A; N/A	1.30; N/A	16.3; N/A	80.2; N/A	17.0; N/A	Tianqi Niu 2020 ^[105]
ITO/NiO _x /CsPbI _x Br _{3-x} -6TIC-4F/ZnO/C ₆₀ /Ag (6TIC-4F surface passivation)	1.78; 1.815	1.16; 76.1%	17.70; 91.7%	78.6; 85.9%	16.10; 59.8%	Jing Wang 2020 ^[104]
ITO/NiO _x /CsPbI _x Br _{3-x} -6TIC-4F/ZnO/C ₆₀ /Ag (6TIC-4F surface passivation)	1.78; 1.815	1.145; 75.1%	17.44; 90.3%	78; 85.2%	15.6; 57.9%	Jing Wang 2020 (certified) ^[104]
FTO/TiO ₂ /β-CsPbI _{2.85} Br _{0.149} Cl _{0.001} /spiro-OMeTAD/Au (In-situ hot oxygen cleansing and passivation)	1.71; 1.722	1.23; 85.5%	19.94; 91.3%	80.11; 87.9%	19.65; 68.6%	Kang Wang 2021 ^[28]

PSC with η of 11.1% and η/η^{SQ} of 53.9%.^[56] As the bandgap is relatively wide for pristine CsPbI₂Br₂ devices, many publications have mainly focused on narrowing the bandgap by Sn-doping and co-absorber layer processes. These devices normally exhibit higher J_{sc} and η but lower $J_{\text{sc}}/J_{\text{sc}}^{\text{SQ}}$ and η/η^{SQ} values. The optimal PSC with a η of 11.53% was achieved by Sn-doping accompanying with low annealing temperature (150 °C).^[123] As for high-quality CsPbBr₃-based perovskite solar cells, we find that the ratios of η/η^{SQ} exhibit high values above 60%, which is much better than that of CsPbI₂Br₂-based devices. Meanwhile, the average FF/FF^{SQ} ratio is as high as around 90%. However, all $V_{\text{oc}}/V_{\text{oc}}^{\text{SQ}}$ values are less than 82%. Yuan et al. have prepared CsPbBr₃ perovskite solar cells with PCE of 10.26%, with an optimal η/η^{SQ} of 67.0% in this group.^[59] Additionally, Duan et al. have reported the champion PCE of 10.85%.^[31] However, due to the lack of EQE dataset, we are not able to make a further analysis.

3.4.2. Performance Variation As a Function of Transport Layer

In this section, we analyze the device performance depending on the types of ETL and HTL materials. To be specific, the ETL materials have been classified into 5 groups: TiO₂, SnO₂, ZnO,

m-TiO₂/c-TiO₂ and others; while the HTLs have been classified into spiro-MeOTAD, NiO_x, other organics, other inorganics and HTL-free. The power conversion efficiency distributions with different transport layers are shown in **Figure 12** as well as Figure S4–S8 (with more details) in Supporting Information (Section 3). As shown in Figure 12a, ETL materials are dominated by inorganic films, especially the TiO₂ and SnO₂ films. For HTLs, a larger variety of materials have been used (Figure 12b). Specifically, spiro-MeOTAD films play a leading role for perovskites with smaller E_g^{ip} , while more inorganic materials or HTL-free structure have been adapted for larger E_g^{ip} perovskite devices.

With regard to CsPbI₃ perovskite solar cells, all the samples have been fabricated with a regular planar structure and have employed spiro-MeOTAD as HTLs. In terms of ETLs, the majority of publications used TiO₂ films, including the champion 20.37% PCE reported by Yoon et al.^[25] and 20.08% PCE reported by Yu et al.^[41] Furthermore, Chang et al. have used SnO₂ ETL and achieved 19% PCE. As for the CsPbI_xBr_{3-x} (2 < x < 3) group, SnO₂ films have been used as ETLs for most of the devices. Nevertheless, the optimal 19.65% PCE has been achieved by utilizing TiO₂ ETL.^[28] ZnO ETL for inverted planar PSC has been reported by Wang et al.^[104] Furthermore, spiro-MeOTAD films have been the predominantly used HTL

Table 3. Performance indicators of reported high-quality CsPbI₂Br ($x = 2$) solar cells. Abbreviations: TL: transport layer, ATS: green anti-solvent, GTA: gradient thermal annealing, PBAI: phenylbutylammonium iodide, EDEA: 2,2'-(ethylenedioxy)diethylamine, PDCBT: poly[5,5'-bis(2-butyloctyl)-(2,2'-bithiophene)-4,4'-dicarboxylate-*alt*-5,5'-2,2'-bithiophene], poly(DTSTPD-*r*-BThTPD): poly[(dithieno[3,2-b:2',3'-d]silolethieno[3,4-c]pyrrole-4,6-dione)-*random*-(2,2'-bithiophenethieno[3,4-c]pyrrole-4,6-dione)], PDTDT: poly[(4,4''-bis(2-ethylhexyl)dithieno[3,2-b:2'',3''-d]silolethieno[3,4-c]pyrrole-4,6-dione)].

Structure (key technology)	$E_{\text{g}}^{\text{rep}}$ [eV]; E_{g}^{ip} [eV]	V_{oc} [V]; $V_{\text{oc}}/V_{\text{oc}}^{\text{SQ}}$	J_{sc} [mA cm ⁻²]; $J_{\text{sc}}/J_{\text{sc}}^{\text{SQ}}$	FF [%]; FF/FF ^{SQ}	η [%]; η/η^{SQ}	Ref.
ITO/c-TiO ₂ /α-CsPbI ₂ Br/ spiro-MeOTAD/Au (ATS/GTA- controlled crystal growth)	N/A; 1.890	1.23; 76.9%	16.79; 98.1%	77.81; 84.7%	16.07; 63.9%	Weijie Chen 2019 ^[42]
ITO/SnO ₂ /CsPbI ₂ Br:CsBr/ spiro-OMeTAD/Au (Interface engineering and Pb(Ac) ₂ additive)	≤1.88; N/A	1.271; N/A	16.72; N/A	77.18; N/A	16.37; N/A	Yuqing Zhang 2019 ^[128]
FTO/TiO ₂ /CsPbI ₂ Br:CuBr/ spiro-OMeTAD/MoO ₃ /Ag (B-site Cu-element doping)	1.95; 1.898	1.18; 73.8%	16.95; 99.0%	80; 87.1%	16.15; 64.2%	Kai-Li Wang 2019 ^[43]
ITO/SnO ₂ /PN ₄ N/CsPbI ₂ Br/ PDCBT/MoO ₃ /Ag (Interface engineering)	N/A; 1.907	1.30; 80.8%	15.3; 90.7%	81.5; 88.7%	16.2; 65.0%	Jingjing Tian 2019 ^[44]
ITO/Cs ₂ CO ₃ :ZnO/CsPbI ₂ Br/ spiro-OMeTAD/MoO ₃ /Ag (ETL doping)	N/A; 1.862	1.28; 81.5%	16.34; 91.3%	78.5; 85.6%	16.42; 63.7%	En-Chi Shen 2020 ^[45]
FTO/c-TiO ₂ /m-TiO ₂ / CsPb _{0.995} Nb _{0.005} I ₂ Br/P3HT/Au (Nb doping and hot air method)	N/A; 1.899	1.315; 82.2%	16.25; 94.9%	77; 83.9%	16.45; 65.4%	Jyoti V. Patil 2020 ^[46]
FTO/c-TiO ₂ /m-TiO ₂ / Cs _{0.99} Rb _{0.01} PbI ₂ Br/P3HT/Au (Rb doping and hot air method)	N/A; 1.899	1.32; 82.5%	16.25; 94.9%	80.03; 87.2%	17.16; 68.2%	Jyoti V. Patil 2020–2 ^[47]
ITO/EDEA/ZnO/CsPbI ₂ Br/PBAI/ spiro-OMeTAD/MoO ₃ /Ag (EDEA and PBAI interface layers)	N/A; 1.903	1.3; 80.8%	15.93; 94.5%	80.2; 87.3%	16.6; 66.6%	Yu-Xin Luo 2020 ^[48]
ITO/ZnO/CsPbI ₂ Br/PolyTPD/ MoO ₃ /Ag (Organic ligands armored ZnO TL)	1.92; 1.887	1.24; 78.0%	16.54; 95.3%	82.1; 89.4%	16.84; 66.5%	Pang Wang 2020 ^[49]
ITO/SnO _x /CsPbI ₂ Br/ poly(DTSTPD- <i>r</i> -BThTPD/Au (SnCl ₂ precursor solution aging)	1.91; 1.881	1.41; 88.7%	14.25; 82.1%	77; 83.9%	15.53; 61.3%	Zhanglin Guo 2020 ^[50]
ITO/SnO ₂ /CsPbI ₂ Br/PTAA/Au (Intermediate-adduct-assisted growth)	N/A; 1.897	1.26; 78.8%	16.95; 99.0%	75; 81.7%	16.02; 63.7%	Min Wang 2021 ^[51]
ITO/SnO ₂ /SnO _x /CsPbI ₂ Br/ PDTDT/Au (dopant-free HTM)	1.91; 1.880	1.42; 89.3%	15.02; 86.5%	81.29; 88.6%	17.36; 68.5%	Zhanglin Guo 2021 ^[29]

materials for regular planar perovskite solar cells, while the NiO_x films have been commonly used as HTLs for inverted planar perovskite solar cells. For the CsPbI₂Br perovskite solar cells, the kinds of ETL and HTL materials are diverse relative to the above two groups. All of the TiO₂, SnO₂, ZnO and m-TiO₂/c-TiO₂ films have been used as ETLs for high performance perovskite solar cells. Guo et al. have prepared modified SnO₂ ETL for CsPbI₂Br perovskite solar cells and achieved the optimal PCE of 17.36% and V_{oc} as high as 1.42 V with a E_{g}^{ip} of 1.88 eV.^[29] Patil et al. have applied m-TiO₂/c-TiO₂ ETL for mesoscopic perovskite solar cells and obtained the PCE of 17.16%.^[47] In addition, though spiro-MeOTAD has still been the predominant HTL material, other organic HTL materials, such as PDTDT, P3HT, poly(*N,N'*-bis-4-butylphenyl-*N,N'*-bisphenyl)benzidine (PolyTPD) and PTAA, have also shown satisfying performance. The perovskite

solar cells which utilized PDTDT, P3HT and PolyTPD as HTLs have reached PCE of 17.36%,^[29] 17.16%^[47] and 16.84%^[49] respectively, higher than that of 16.6%^[48] using spiro-MeOTAD film. Regarding CsPbI₂Br and CsPbI_{1.5}Br_{1.5} perovskite solar cells, we find that both TiO₂ and SnO₂ films have been generally used relative to the others, among which TiO₂ containing perovskite solar cells exhibited better performance in terms of PCE. As for HTLs, besides of the predominantly used spiro-MeOTAD films, inorganic NiO_x,^[30] (NiCo)_{1-y}Fe_yO_x-GO^[57] materials and carbon-electrode-based HTL-free perovskite solar cells^[52,54] have also been reported. For the CsPbBr₃ group, m-TiO₂/c-TiO₂, TiO₂, and SnO₂ have been the main ETLs, while there is little performance difference among these devices. In addition, the carbon-electrode-based HTL-free structure is the most popular device geometry for CsPbBr₃ perovskite solar cells. Based on this,

Table 4. Performance indicators of reported high-quality CsPbI_{1.5}Br_{1.5} ($x = 1.5$) and CsPbIBr₂ ($x = 1$) solar cells. Abbreviations: TL: transport layer, PEG: poly(ethylene glycol), FITC: fluorescein isothiocyanate, MA: methylammonium, PEI: polyethylenimine, SAS: sodium salt, YD₂-o-C₈: 5,15-bis(2,6-dioctoxyphenyl)-10-(bis(4-hexylphenyl)-amino-20-4-carboxyphenylethynyl)porphyrinatozinc(II).

Structure (key technology)	E_g^{exp} [eV]; E_g^{ip} [eV]	V_{oc} [V]; $V_{\text{oc}}/V_{\text{oc}}^{\text{SQ}}$	J_{sc} [mA cm ⁻²]; $J_{\text{sc}}/J_{\text{sc}}^{\text{SQ}}$	FF [%]; FF/FF ^{SQ}	η [%]; η/η^{SQ}	Ref.
FTO/SnO ₂ /ZnO/CsPbI _{1.5} Br _{1.5} /spiro-OMeTAD/Au (FITC additive)	1.96; 1.956	1.29; 77.9%	14.1; 90.3%	77.1; 83.8%	14.05; 59.0%	Weihai Zhang 2020 ^[106]
FTO/c-TiO ₂ /m-TiO ₂ /CsPb _{0.9} Sn _{0.1} Br ₂ /carbon (B-site Sn-element doping)	1.79; 1.876	1.26; 79.7%	14.3; 81.2%	63; 68.7%	11.33; 44.3%	Jia Liang 2017 ^[129]
ITO/SnO ₂ /C ₆₀ /CsPb _{0.75} Sn _{0.25} Br ₂ /spiro-OMeTAD/Au (B-site Sn-element doping)	1.78; 1.905	1.21; 75.2%	12.57; 74.6%	75.8; 82.5%	11.53; 46.3%	Nan Li 2018 ^[123]
FTO/c-TiO ₂ /CsPbIBr ₂ /carbon (Intermolecular exchange strategy)	2.05; 2.130	1.24; 68.3%	10.66; 89.1%	69; 74.5%	9.16; 45.5%	Weidong Zhu 2018 ^[52]
ITO/SnO ₂ /SnCl ₂ /CsPbIBr ₂ /YD ₂ -o-C ₈ /spiro-OMeTAD/Au (co-sensitization layer and interface passivation)	2.05; 1.961	1.37 82.3%	12.05; 78.3%	61; 66.2%	10.13; 42.9%	Shuzhang Yang 2019 ^[130]
FTO/TiO ₂ /CsPb(Ba)IBr ₂ /Spiro-OMeTAD/Au (B-site Ba-element doping)	2.11–2.12; 2.097	1.19; 66.5%	11.91; 94.9%	74; 80.0%	10.51; 50.6%	Waqas Siddique Subhani 2019 ^[131]
FTO/TiO ₂ /SmBr ₃ /CsPbIBr ₂ /spiro-OMeTAD/Au (SmBr ₃ interface modification)	2.14; 2.100	1.17; 65.4%	12.75; 101.6%	73; 78.9%	10.88; 52.4%	Waqas Siddique Subhani 2019-2 ^[53]
FTO/TiO ₂ /CsBr/CsPbIBr ₂ /carbon (CsBr interface modification)	2.04; 2.108	1.261; 70.1%	11.8; 95.4%	72; 77.8%	10.71; 52.1%	Weidong Zhu 2019 ^[54]
FTO/TiO ₂ /CsPb(SO ₃)IBr ₂ /spiro-OMeTAD/Au (SAS additive)	2.1; 2.066	1.21; 68.7%	12.27; 93.2%	71; 76.8%	10.57; 49.4%	Yulong Wang 2020 ^[132]
FTO/SnO ₂ /CsPbIBr ₂ /spiro-OMeTAD/Au (MABr Seed-Assisted Growth method)	N/A; N/A	1.24; N/A	12; N/A	74.6; N/A	11.1; N/A	Weihai Zhang 2020 ^[55]
FTO/SnO ₂ /Cs _{0.99} MA _{0.01} PbIBr ₂ /spiro-OMeTAD/Au (MABr Seed-Assisted Growth method, low-T process)	2.11; 2.130	1.21; 66.6%	11.94; 99.7%	72.5; 78.3%	10.47; 52.0%	Weihai Zhang 2020–2 ^[55]
FTO/TiO ₂ /CsPbIBr ₂ :PEG/spiro-OMeTAD/Ag (Lewis base (PEG) additive)	2.07; 2.108	1.21; 67.3%	12.25; 99.0%	74.82; 80.8%	11.1; 53.9%	Yibo You 2020 ^[56]
FTO/SnO ₂ /CsPbIBr ₂ :PEI/NiO _x /Au (PEI additive)	2.01; 1.803	1.25; 82.5%	13.30 68.0%	68; 74.3%	11.3; 41.7%	Bowen Gao 2020 ^[30]
FTO/c-TiO ₂ /CsPbIBr ₂ /(NiCo) _{1-y} Fe _y O _x -GO/carbon (TL design)	2.09; 2.115	1.29; 71.4%	12.03; 98.8%	70.58; 76.2%	10.95; 53.8%	Jian Du 2021 ^[57]

various kinds of new inorganic transport layer materials have been investigated, including NiO_x,^[59] MnS,^[61] Cu(Cr,Ba)O₂ NCs,^[60] CuInS₂/ZnS QDs^[31] and Br-GO GO.^[109] However, though the utilization of new transport layer materials have achieved favorable performance, they show a limited effect (with PCE just increase from 10.14% to 10.85%, less than 1%) and thus more efforts are still urgently needed.

3.4.3. Surface and Interface Passivation

Tables 1–5 list the key aspects of the device stack and the processing condition that define the unique aspects of the different publications. We observe that surface and interface passivation

methods are among the most frequently used strategies to improve performance beyond the state of the art. Especially, in hybrid lead-halide perovskites, the detrimental effect of surfaces and interfaces leading to enhanced carrier recombination, short photoluminescence lifetimes and lower external luminescence quantum efficiencies as well as open-circuit voltages has been thoroughly investigated.^[134] Defect passivation could effectively reduce the defect density at the surfaces/interfaces, which has been of major importance for the device performance improvement of hybrid^[135] but also all-inorganic perovskite solar cells in recent years. The passivation techniques applied to all-inorganic perovskite solar cells include the following types, 1) Induced 2D layers: It has been reported that OAI,^[25] PEAI^[40] and GABr^[122] could have a passivation effect due to the formation of a 2D

Table 5. Performance indicators of reported high-quality CsPbBr₃ ($x = 0$) solar cells. Abbreviations: TL: transport layer, LPP: long persistence phosphor, N-CQDs: nitrogen-doped carbon quantum dots, Br-GO: brominated graphene oxide.

Structure (key technology)	E_g^{rep} [eV]; E_g^{ip} [eV]	V_{oc} [V]; V_{oc}/V_{oc}^{SQ}	J_{sc} [mA cm ⁻²]; J_{sc}/J_{sc}^{SQ}	FF [%]; FF/FF ^{SQ}	η [%]; η/η^{SQ}	Ref.
FTO/c-TiO ₂ /m-TiO ₂ /CsPb _{0.97} Sm _{0.03} Br ₃ / carbon (Sm doping)	N/A; 2.319	1.594; 79.9%	7.48; 86.3%	85.1; 91.4%	10.14; 62.9%	Jialong Duan 2018 ^[58]
FTO/c-TiO ₂ /m-TiO ₂ /CsPb _{0.97} Tb _{0.03} Br ₃ /SnS:ZnS/NiO _x / carbon (Integrated solar cell)	2.3; 2.360	1.57; 77.2%	8.21; 101.7%	79.6; 85.4%	10.26; 67.0%	Haiwen Yuan 2018 ^[59]
FTO/SnO ₂ /CsPbBr ₃ /CsSnBr ₃ QDs/ carbon (TL design)	2.3; N/A	1.61; N/A	7.80; N/A	84.4; N/A	10.60; N/A	Yuanyuan Zhao 2019 ^[133]
FTO/TiO ₂ /CsPb _{0.97} Sm _{0.03} Br ₃ / Cu(Cr,Ba)O ₂ NCs/Carbon (Sm doping and TL design)	N/A; N/A	1.62; N/A	7.81; N/A	85.5; N/A	10.79; N/A	Jialong Duan 2019 ^[60]
FTO/TiO ₂ /CsPbBr ₃ /Cu(Cr,Ba)O ₂ NCs/ carbon (TL design)	2.34-2.35; 2.279	1.602; 81.8%	7.62; 81.9%	83.4; 89.6%	10.18; 60.0%	Jialong Duan 2019 ^[60]
FTO/c-TiO ₂ /m-TiO ₂ /CsPbBr ₃ / MnS/ carbon (vapor-assisted solution technique and TL design)	2.3; 2.293	1.52; 76.9%	8.28; 92.2%	83; 89.2%	10.45; 63.2%	Xin Li 2019 ^[61]
FTO/SnO ₂ /CsPbBr ₃ /carbon (grain growth control)	N/A; 2.361	1.588; 78.11%	7.64; 94.7%	84.1; 90.2%	10.2; 66.7%	Yuanyuan Zhao 2020 ^[62]
FTO/c-TiO ₂ /m-TiO ₂ /CsPbBr ₃ / CuInS ₂ / ZnS QDs/LPP-C (TL and electrode design)	2.3; N/A	1.626; N/A	7.73; N/A	86.3; N/A	10.85; N/A	Jialong Duan 2020 ^[31]
FTO/c-TiO ₂ /m-TiO ₂ /CsPbBr ₃ :Br-GO/Br-GO/carbon (Br-GO additive and HTL)	2.34; N/A	1.602; N/A	7.88; N/A	80.01; N/A	10.10; N/A	Xuemiao Sun 2021 ^[109]

perovskite layers on the surface of 3D perovskite films. 2) Post treatments: The addition of PTABr,^[36] CHI,^[26] PTACI,^[37] 6TIC-4F^[104] and CsBr^[128] has been used for perovskite surface treatment to passivate defects. 3) Interfacial layers: The preparation of interfacial layers, e.g., LiF,^[125] EDEA^[48] and PBAI,^[48] between perovskite and transport layer has been proven to be effective in defect passivation. Nevertheless, improper surface/interface passivation may cause an increase of the series resistance R_s , or even interface deterioration, and thus can lead to a reduced J_{sc} and FF. It should be noted that passivation can not only reduce defect density and improve device performance, but also enhance the stability simultaneously. For instance, 2D

perovskite layer capping can improve V_{oc} due to the passivation effect as well as prevent moisture and oxygen ingress by forming a compact layer on the surface of the 3D perovskite.^[25,38,40,122] In addition, as mentioned above, CsPbI₃ exhibits a relatively low tolerance factor which means phase transitions may easily occur. Fortunately, it has been demonstrated that interface passivation can effectively enhance the phase stability. Zhao and coworker have reported that using PTABr,^[36] CHI,^[26] and PTACI^[37] reagents can passivate surface defects and improve the phase stability of CsPbI₃ perovskites at the same time. Introduction of hydrophobic groups on perovskite surface can further prevent moisture penetration. Apart from that, lowering

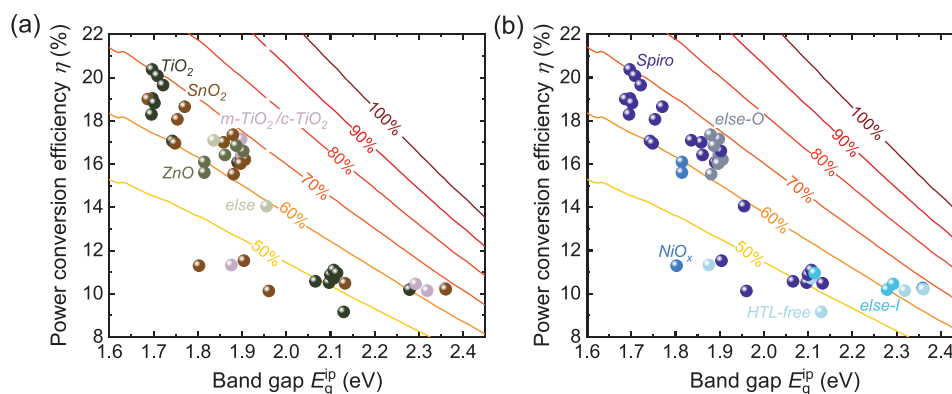


Figure 12. a,b) The power conversion efficiencies distribution with respect to E_g^{ip} of the all-inorganic perovskite solar cells, of which datapoints are encoded by ETL (a) and HTL (b) materials. The colored lines illustrate the percentage of SQ limits

the surface energy by interface engineering is also promising strategy for improving the phase stability of CsPbI₃.^[136]

4. Loss Analysis

4.1. Overview

In this section, we analyse the loss sources and the underlying physical mechanisms for all-inorganic perovskites. As discussed in last chapter, we find that the V_{oc}/V_{oc}^{SQ} values of most of the present all-inorganic perovskite solar cells are at a relatively low level, indicating that the performance is mainly restricted by substantial voltage losses. **Figure 13** shows the distribution of V_{oc} along with E_g^{ip} for the high-quality all-inorganic perovskite solar cells. The colored reference lines represent the radiative limit of open-circuit voltage V_{oc}^{rad} for different external luminescence quantum efficiencies Q_e^{lum} (10^{-14} to 1) calculated with a step function, which is useful to better reveal the actual level of V_{oc} under different bandgaps. Among all-inorganic perovskite solar cells, the CsPbBr₃ devices exhibit the maximum V_{oc} , for which could reach 1.6 V. Such high value of V_{oc} is mostly responsible by the wide bandgaps. The corresponding Q_e^{lum} in the range of 10^{-6} to 10^{-8} has been attained, which has no advantages over other perovskite solar cells. In terms of Q_e^{lum} , the CsPbI₃ and CsPbI_xBr_{3-x} ($2 < x < 3$) perovskite solar cells exhibit the optimal values, which could approach 10^{-2} and 10^{-3} respectively. However, there is still a gap compared with the highly efficient hybrid perovskite solar cells. For instance, Liu et al. have obtained a $Q_e^{lum} \approx 5\%$ for completed MAPb(I_{0.8}Br_{0.2})₃ perovskite solar cells ($E_g = 1.725$ eV) with 1.35 V V_{oc} , which is higher than any all-inorganic perovskite solar cells.^[88] Noting that all the

Q_e^{lum} values mentioned here were based on completed devices and thus these values were lower than those reported by other publications which were obtained from perovskite films.^[88] For CsPbI₃ perovskite solar cells, Ye et al. have fabricated 3D/2D mixed CsPbI₃ devices achieving an optimal V_{oc} of 1.33 V under 1.749 eV E_g^{ip} ,^[38] as well as a calculated $Q_e^{lum} \approx 1.13\%$ which is the highest value among the discussed all-inorganic perovskite solar cells. It is worth noting that the position of this data point in the figure is slightly lower than the reference line of $Q_e^{lum} = 1\%$. This situation also happens to some other samples. Such difference could be attributed to the non-negligible radiative recombination for actual devices, which cannot be taken into account in the calculation of the reference lines. For the recorded device (PCE = 20.37%) reported by Yoon et al.,^[25] the Q_e^{lum} is calculated to be $\approx 0.042\%$. Zheng et al. have achieved the optimal $Q_e^{lum} \approx 0.21\%$ among the CsPbI_xBr_{3-x} ($2 < x < 3$) group with a relatively low bandgap of 1.754 eV.^[122] The maximum Q_e^{lum} value for CsPbI₂Br group is calculated to be $\approx 0.54\%$ using the results reported by Guo et al.^[29] As for CsPbIBr₂ perovskite solar cells, Yang et al. have designed novel transport layers to narrow down the bandgap to 1.961 eV (obviously lower than the intrinsic value) and obtained a high 1.32 V V_{oc} ,^[130] resulting in an optimal Q_e^{lum} of $\approx 0.013\%$. In terms of the CsPbIBr₂ perovskite solar cells with bandgap close to the intrinsic value, Du et al. have demonstrated a maximum $V_{oc} = 1.29$ V with $E_g^{ip} = 2.115$ eV^[57] as well as an extremely small $Q_e^{lum} \approx 6.0 \times 10^{-7}\%$, suggesting great potential of V_{oc} improvement for CsPbIBr₂ perovskite solar cells. With regard to CsPbBr₃ perovskite solar cells, the optimal $Q_e^{lum} \approx 2.7 \times 10^{-4}\%$ has been achieved by Duan et al.^[60]

By utilizing the inflection point of the external quantum efficiency as the bandgap for the related perovskite solar cells, we can now reliably compare and analyze energy losses for all-inorganic perovskite solar cells in a unified method. There are two loss terms for the actual open-circuit voltage V_{oc} , i.e., the radiative loss ΔV_{oc}^{rad} and the nonradiative loss ΔV_{oc}^{nonrad} . According to the calculation method introduced in Supporting Information (Section 1.3), we calculated the radiative open-circuit voltage V_{oc}^{rad} , ΔV_{oc}^{rad} and ΔV_{oc}^{nonrad} for each of the devices. The corresponding results are listed in Tables S3–S7 in Supporting Information (Section 5). The ΔV_{oc}^{nonrad} therein originates from the nonradiative recombination in the bulk and at the interfaces, which has been widely focused on by the academic community and can be suppressed by film quality improvement and interface optimization. **Figure 14a** provides an overview over the distribution of ΔV_{oc}^{nonrad} along with E_g^{ip} value, which presents a raising tendency with widening E_g^{ip} . CsPbIBr₂-based perovskite solar cells exhibit the maximum nonradiative loss ΔV_{oc}^{nonrad} . In particular, for the devices with E_g^{ip} close to the intrinsic value of CsPbIBr₂ (≈ 2.1 eV), the calculated ΔV_{oc}^{nonrad} is as high as 450–600 mV. CsPbI₃-based, CsPbI_xBr_{3-x}-based ($2 < x < 3$) and CsPbI₂Br perovskite solar cells present relatively lower ΔV_{oc}^{nonrad} , which can be lower than 200 mV. Nevertheless, such nonradiative loss is still pretty large compared with high-quality hybrid perovskite solar cells, whose ΔV_{oc}^{nonrad} can be suppressed to below 100 mV.^[88,137,138] **Figure 14b** presents the limitation of J_{sc}/J_{sc}^{SQ} value with respect to ΔV_{oc}^{nonrad} for all-inorganic perovskite solar cells. Obviously, there is a negative correlation between current loss and voltage loss, which means that it is difficult to achieve a low current loss and a low voltage loss at the same time.

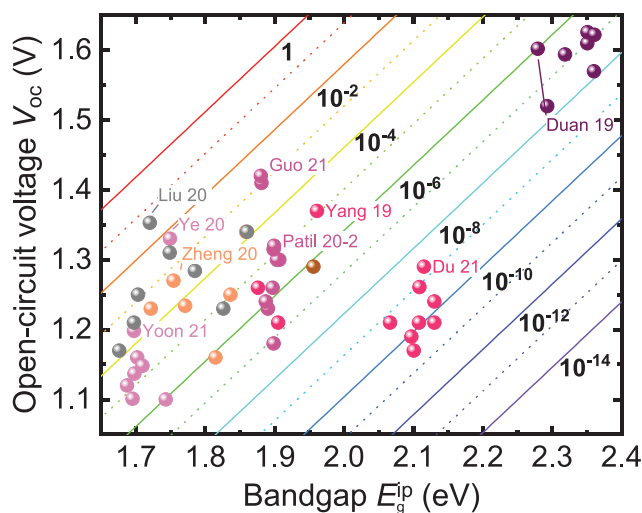


Figure 13. Open-circuit voltages V_{oc} of all-inorganic perovskite solar cells versus E_g^{ip} . The high-quality organic hybrid perovskite solar cells are also shown in figure for comparison. The reference lines illustrate the external luminescence quantum efficiency (10^{-14} to 1) calculated with a step function. Each color represents a group of CsPbI_xBr_{3-x} perovskite solar cells (plum: CsPbI₃-based perovskite solar cells; orange: CsPbI_xBr_{3-x}-based ($2 < x < 3$) perovskite solar cells; violet: CsPbI₂Br-based perovskite solar cells; sienna: CsPbI_{1.5}Br_{1.5}-based PSC; deep pink: CsPbIBr₂-based perovskite solar cells; purple: CsPbBr₃-based perovskite solar cells; gray: hybrid perovskite solar cells).

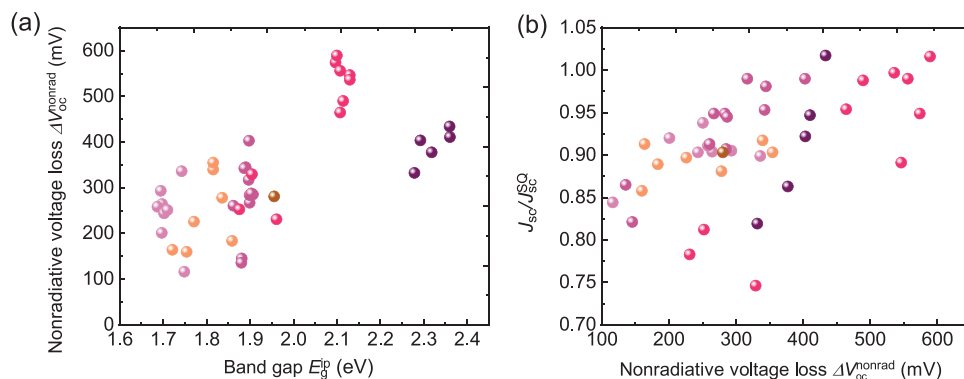


Figure 14. a) Overview of nonradiative V_{oc} loss ΔV_{oc}^{nonrad} distribution along with E_g^{ip} . b) Comparison of the limitations of the present high-quality all-inorganic perovskite solar cells from the literature. The performance with regard to the short-circuit current density is indicated by the ratio of experimental J_{sc} compared to the corresponding value in the SQ model J_{sc}^{SQ} . Each color of the datapoints represents one group of all-inorganic $CsPbI_xBr_{3-x}$ -based perovskite solar cells (plum: $CsPbI_3$ -based perovskite solar cells; orange: $CsPbI_xBr_{3-x}$ -based ($2 < x < 3$) perovskite solar cells; violet: $CsPbI_2Br$ -based perovskite solar cells; sienna: $CsPbI_{1.5}Br_{1.5}$ -based PSC; deep-pink: $CsPbIBr_2$ -based perovskite solar cells; purple: $CsPbBr_3$ -based perovskite solar cells).

Though the voltage loss is high for $CsPbIBr_2$ -based perovskite solar cells as mentioned above, they exhibit a low current loss. The $CsPbI_3$ -based and $CsPbI_xBr_{3-x}$ -based ($2 < x < 3$) perovskite solar cells present a higher current loss, which could be attributed to the V_{oc} optimization process. For instance, interface passivation is an effective mechanism to reduce ΔV_{oc}^{nonrad} , which would increase series resistance at the same time because of the addition of dielectric interface layer and in consequence has a negative effect on the short-circuit current density J_{sc} .

There are several possible reasons for the relatively high J_{sc}/J_{sc}^{SQ} ratios of perovskite solar cells with larger bandgap (e.g., $CsPbI_2Br$): 1) Absorption below E_g^{ip} . We compare the absorption of an ideal step function with a step at E_g^{ip} to calculate SQ limit with the actually measured EQE spectra. For bandgaps substantially above the maximum of the efficiency versus bandgap curve predicted by the SQ model, the below E_g^{ip} absorption becomes relatively more important. 2) Measurement errors. We find frequent disagreements between the stated J_{sc} from $J-V$ curves compared to the J_{sc} obtained from the integration of the EQE spectrum. We will discuss it later (Section 4.7). Furthermore, the calibration of the solar simulator is often done with Si photodiodes. Given that the risk of calibration and measurement errors increases if the bandgap of the device under test and the reference photodiode are different,^[139] it is conceivable that the occurrence of measurement errors increases for higher bandgaps.

In the following, we break down the efficiency losses into five figure of merits (FoMs) to reveal the physical mechanism via the following equation,^[6,140]

$$\frac{\eta^{real}}{\eta^{SQ}} = F_{sc} \frac{V_{oc}^{real}}{V_{oc}^{rad}} \frac{V_{oc}^{rad}}{V_{oc}^{SQ}} \frac{FF_0(V_{oc}^{real})}{FF_0(V_{oc}^{SQ})} F_{FF}^{res} \quad (9)$$

where $F_{sc} = J_{sc}^{real}/J_{sc}^{SQ}$ and $F_{FF}^{res} = FF_0^{real}/FF_0(V_{oc}^{real})$. $FF_0(V_{oc})$, the value without resistive losses, can be calculated as following,^[6,140]

$$FF_0 = \frac{\frac{qV_{oc}}{n_{id}kT_{cell}} - \ln\left(\frac{qV_{oc}}{n_{id}kT_{cell}} + 0.72\right)}{\frac{qV_{oc}}{n_{id}kT_{cell}} + 1} \quad (10)$$

The corresponding physical loss mechanisms are shown in Table 6. The details have been introduced in the Supporting Information (Section 1.4). Figure 15 presents the energy loss comparison of the representative all-inorganic perovskite solar cells in each group. There are also three high-quality hybrid perovskite solar cells with low ΔV_{oc}^{nonrad} shown for comparison. We find that all-inorganic perovskite solar cells present larger energy losses compared with the hybrid perovskite solar cells. Especially, the $CsPbIBr_2$ -based perovskite solar cells possess the largest energy losses, following by $CsPbI_{1.5}Br_{1.5}$ -based and $CsPbBr_3$ -based perovskite solar cells, whose η/η^{SQ} values are much lower than that of hybrid perovskite solar cells. For the $CsPbI_3$ and $CsPbI_xBr_{3-x}$ ($2 < x < 3$) devices, the related η/η^{SQ} values tend to be close to hybrid perovskite solar cells, benefiting from the similar or even smaller loss in F_{FF}^{res} . However, there is still large room to catch up with the hybrid devices with respect to the $V_{oc}^{real}/V_{oc}^{rad}$ loss. For the complete set of all-inorganic perovskite solar cells shown, the energy losses are dominated by the FoMs of $V_{oc}^{real}/V_{oc}^{rad}$ and F_{FF}^{res} , indicating severe non-radiative recombination loss, high series resistance and poor ideality factor. In addition, for the devices with $x > 2$, the F_{sc} , which is due to the photocurrent loss, also accounts for a large proportion of the total efficiency loss. Nevertheless, its effect would be weakened along with increasing of bandgap energy, while the effect of $V_{oc}^{real}/V_{oc}^{rad}$ factor would become stronger. In

Table 6. Figure of merits used for performance loss analysis and the corresponding physical loss mechanisms of perovskite solar cells.

Figure of merit	Physical loss mechanism
$F_{sc} = J_{sc}/J_{sc}^{SQ}$	Photocurrent loss.
$FF_0(V_{oc}^{real})/FF_0(V_{oc}^{SQ})$	FF loss due to the loss in V_{oc} .
$F_{FF}^{res} = FF_0^{real}/FF_0(V_{oc}^{real})$	FF loss due to the resistive and ideality factor.
$V_{oc}^{real}/V_{oc}^{rad}$	V_{oc} loss due to the nonradiative recombination.
$V_{oc}^{real}/V_{oc}^{SQ}$	V_{oc} loss due to discrepancy between the actual absorption coefficient and the assumed step-function in SQ limit.

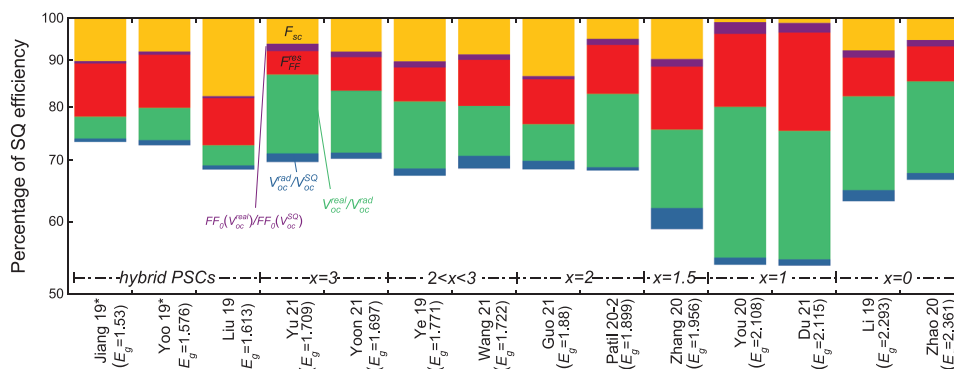


Figure 15. Visualized comparison of potential improvement for the champion all-inorganic perovskite solar cells in each group. High-quality hybrid perovskite solar cells have been taken account of as well.^[137,138] The respective F_{sc} for each device has been marked.

the following, we discuss the physical loss mechanisms for each group of all-inorganic perovskite solar cells in detail.

4.2. CsPbI₃-Based ($x = 3$) Perovskite Solar Cells

Figure 16a shows the comparison of voltage and current losses for CsPbI₃-based perovskite solar cells, i.e., the J_{sc}/J_{sc}^{SQ} value versus nonradiative loss ΔV_{oc}^{nonrad} . The performance of the device from Yoon et al. stands out, and exhibits small losses in both short-circuit current density ($J_{sc}/J_{sc}^{SQ} = 92.0\%$) and open-circuit voltage ($\Delta V_{oc}^{nonrad} = 201$ mV), demonstrating the great advantage of sequential dripping of a methylammonium chloride solution (SDMS) method and octylammonium iodide (OAI) surface passivation technology in balancing current and voltage performance.^[25] The device from Yu et al. also shows good balance between J_{sc} and V_{oc} performance with ΔV_{oc}^{nonrad} of 250.9 mV and J_{sc}/J_{sc}^{SQ} of 93.8%.^[41] Ye et al. obtained an ultralow ΔV_{oc}^{nonrad} of 116 mV by fabricating a 2D/3D mixed-dimensional perovskite structure, which is the lowest value among all the discussed devices in this paper. However, the current performance has been sacrificed for the voltage optimization and the J_{sc}/J_{sc}^{SQ} value was only 84.4%, which is lower than its

competitors.^[38] Apart from this device, we find that the J_{sc}/J_{sc}^{SQ} values are pretty similar among this group and thus the non-radiative voltage loss ΔV_{oc}^{nonrad} is considered as the main factor affecting device performance. In 2021, Liu et al. have achieved a low $\Delta V_{oc}^{nonrad} = 243.5$ mV for the solar cell with structure of 2D capping layer on 3D perovskite which generally comes at the cost of current loss. The J_{sc}/J_{sc}^{SQ} value for their device is still close to other devices in this group.^[40] Chang et al. have developed blade-coating process for PSC with FTO/SnO₂/CsPbI₃:Zn(C₆F₅)₂/CsPbI₃/spiro-OMeTAD/Au structure and obtained a low ΔV_{oc}^{nonrad} of 258.3 mV, demonstrating the great potential of blade-coating process for high-quality perovskite thin films and devices. Wang et al. have focused on surface passivation technique and published some related articles, of which ΔV_{oc}^{nonrad} presented a decreasing trend, from the initial 336 mV to 264.4 mV.^[26,36,37] It is observed that the efficiency of CsPbI₃-based perovskite solar cells has been satisfyingly improved from 17.06% to 20.37% within 3 years, which could be due to the successful optimization for nonradiative voltage loss ΔV_{oc}^{nonrad} .

As shown in **Figure 16b**, the parts of $V_{oc}^{real}/V_{oc}^{rad}$ (green), F_{sc} (yellow) and F_{FF}^{res} (red) make up the main share for present CsPbI₃-based perovskite solar cells, indicating the primary

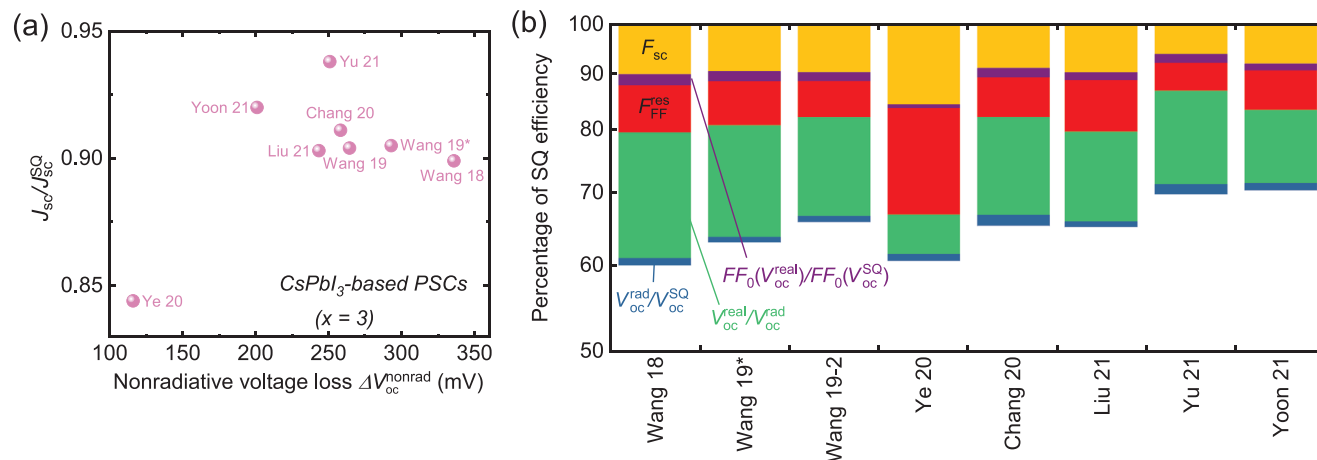


Figure 16. Loss comparison of CsPbI₃-based perovskite solar cells. a) Comparison of the J_{sc}/J_{sc}^{SQ} limitation with respect to nonradiative voltage ΔV_{oc}^{nonrad} . b) Visualization of potential improvement using FoMs of the efficiency losses.

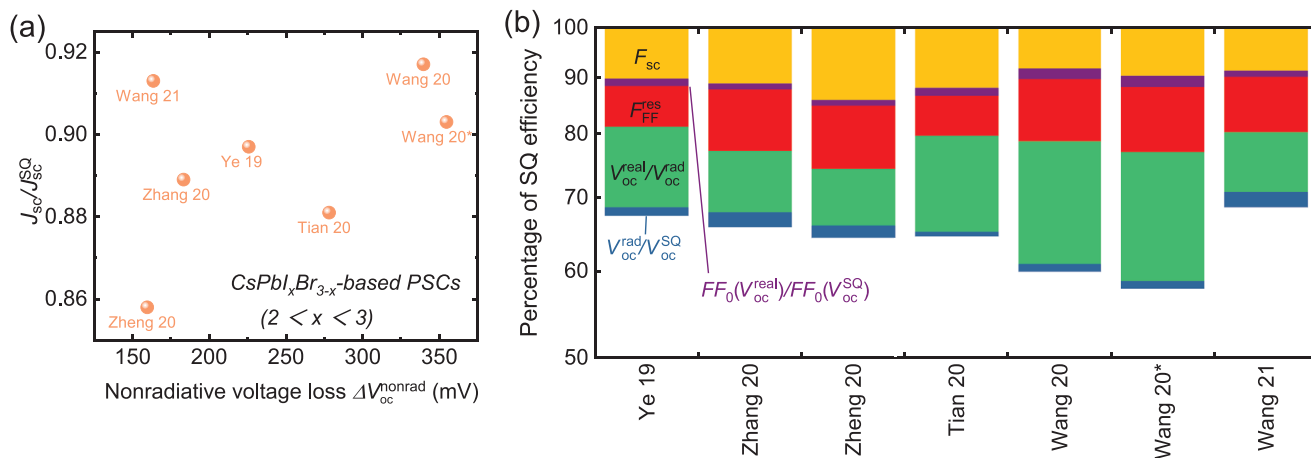


Figure 17. Loss comparison of CsPbI_xBr_{3-x}-based (2 < x < 3) perovskite solar cells. a) Comparison of the J_{sc}/J_{sc}^{SQ} limitation with respect to nonradiative voltage ΔV_{oc}^{nonrad} . b) Visualization of potential improvement using FoMs of the efficiency losses.

losses by nonradiative recombination, photocurrent and series resistance together with ideality factor. By contrast, the green bar is the largest in terms of the area for most devices, namely, the nonradiative voltage loss is the dominant factor for performance difference, indicating that the main strategy for performance improvement should focus on suppressing carrier nonradiative recombination, which is consistent with the above discussion. Although Ye et al. have reported the best $V_{oc}^{real}/V_{oc}^{rad}$ factor, both the F_{sc} and F_{FF}^{res} losses are pretty large compared with the others and thus limits the efficiency. For further performance improvement, efforts on balancing nonradiative voltage loss and resistive loss should be done.

4.3. CsPbI_xBr_{3-x}-Based (2 < x < 3) Perovskite Solar Cells

Figure 17a compares losses for CsPbI_xBr_{3-x}-based (2 < x < 3) perovskite solar cells. Wang et al. (2021) have reported an optimal performance with 68.6% η/η^{SQ} in this group, revealing excellent balance between the ΔV_{oc}^{nonrad} (163.6 mV) and J_{sc}/J_{sc}^{SQ} (91.3%).^[28] Zheng et al. have reported the highest V_{oc}/V_{oc}^{SQ} value of 86.5%, which originates from the ultralow ΔV_{oc}^{nonrad} of 159.6 mV.^[122] Similar to Ye et al.^[38] and Liu et al.^[40] mentioned above, Zheng et al. have also prepared 2D perovskite on the 3D perovskite film in order to optimize the CsPbI_xBr_{3-x}/spiro-OMeTAD interface and consequently reduce nonradiative recombination. However, though the ΔV_{oc}^{nonrad} performs well, the J_{sc}/J_{sc}^{SQ} ratio is relatively low (85.8%), and thus becomes the limiting factor for efficiency improvement. Zhang et al. have demonstrated better balance between voltage loss and current loss for the device with FTO/c-SnO₂/CsPb(I_{0.75}Br_{0.25})₃:FAOAc/spiro-OMeTAD/Au structure, of which ΔV_{oc}^{nonrad} = 183.3 mV and J_{sc}/J_{sc}^{SQ} = 88.9% have been obtained. Different from the former work, Zhang et al. have concentrated on the c-SnO₂/CsPb(I_{0.75}Br_{0.25})₃ interface and achieved the goal of ΔV_{oc}^{nonrad} reduction by introducing FAOAc volatile salts.^[126] These two studies have adopted similar device structures but focused on the upper and lower surfaces of perovskite films respectively and both exhibited favorable effect on reducing nonradiative recombination. There is no obvious conflict of these two

technologies and it seems possible to combine them together to further reduce ΔV_{oc}^{nonrad} , aiming to achieve ΔV_{oc}^{nonrad} that could as low as that for hybrid perovskite solar cells. Ye et al. have focused on SnO₂/perovskite interface as well and prepared a LiF film at the interface for passivation. This device exhibited favorable balance with ΔV_{oc}^{nonrad} = 225.8 mV and J_{sc}/J_{sc}^{SQ} = 89.7%, which is contributed to the 18.64% PCE and 67.3% η/η^{SQ} .^[125] Wang et al. have made efforts on ΔV_{oc}^{nonrad} reduction as they stated, but according to our comparison analysis, they have excelled in short-circuit current density loss as their 91.7% J_{sc}/J_{sc}^{SQ} value comes to the top among this group.^[104] From the FoMs loss analysis shown in Figure 17b, $V_{oc}^{real}/V_{oc}^{rad}$, F_{FF}^{res} and F_{sc} contribute the main share for energy losses. Devices from Wang et al. (2021), Zheng et al. and Zhang et al. have advantages in $V_{oc}^{real}/V_{oc}^{rad}$ ratio, indicating the lower nonradiative recombination loss. Devices from Tian et al. and Ye et al. performed better in F_{FF}^{res} , which represents smaller series resistance and better ideality factor for the devices. While the device from Wang et al. (2020) existed fewer photocurrent loss due to the smaller area of F_{sc} . Similar to CsPbI₃-based perovskite solar cells, a balance between the indicators is the key for further performance improvement.

4.4. CsPbI₂Br-Based (x = 2) Perovskite Solar Cells

The comparison of losses for CsPbI₂Br-based perovskite solar cells is presented in Figure 18a. Guo et al. have developed a new type dopant-free hole-transport material PDTDT for CsPbI₂Br solar cell and obtained the optimal PCE of 17.36% and minimum ΔV_{oc}^{nonrad} of as low as 135.7 meV in this group, whereas the J_{sc}/J_{sc}^{SQ} was limited.^[29] Patil et al. have utilized Nb-doping and Rb-doping process for CsPbI₂Br perovskite solar cells and both obtained favorable comprehensive results.^[46,47] The one proceeding Rb-doping performed better and achieved a ΔV_{oc}^{nonrad} = 266.9 mV and J_{sc}/J_{sc}^{SQ} = 94.9%.^[47] Shen et al. have reported small ΔV_{oc}^{nonrad} of 260.4 mV by utilizing Cs₂CO₃:ZnO ETL.^[45] The devices from Wang et al. (2019),^[43] Wang et al. (2021)^[51] and Chen et al. (2019)^[42] exhibit nice J_{sc}/J_{sc}^{SQ} value, while the ΔV_{oc}^{nonrad} is relatively high,

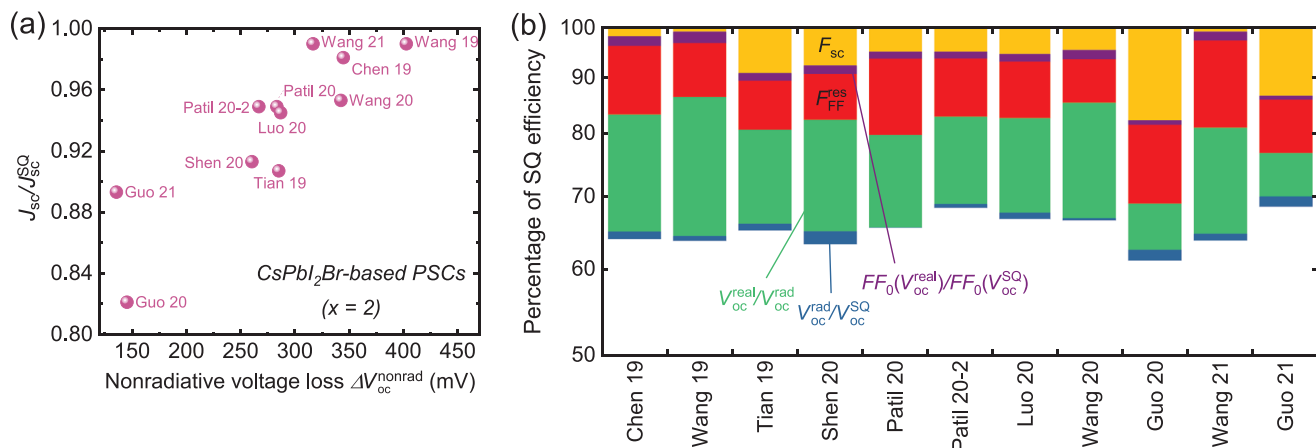


Figure 18. Loss comparison of $CsPbI_2Br$ -based perovskite solar cells. a) Comparison of the J_{sc}/J_{sc}^{SQ} limitation with respect to nonradiative voltage ΔV_{oc}^{nonrad} . b) Visualization of potential improvement using FoMs of the efficiency losses.

indicating that suppression of carrier nonradiative recombination is significant for performance improvement. The related FoMs loss analysis is shown in Figure 18b. On the whole, the green bar is the largest in terms of the area, suggesting that more efforts on suppressing nonradiative recombination should be done. In addition, the distinct red area indicates the deficiency of series resistance and ideality factor for present $CsPbI_2Br$ -based perovskite solar cells. Compared with $CsPbI_xBr_{3-x}$ devices with $x>2$, F_{sc} factor show less impact on $CsPbI_2Br$ perovskite solar cells. In particular, devices from Chen et al. (2019),^[42] Wang et al. (2021)^[51] and Wang et al. (2019)^[43] performed ultralow short-circuit current density loss. In addition, Patil et al.^[46] have achieved the best V_{oc}^{rad}/V_{oc}^{SQ} value by Nb-doping process, demonstrating that the actual shape quantum efficiency is much close to the ideal step-function assumed in the SQ limit. In a brief, apart from the others factors, suppression on nonradiative recombination loss is the primary task for $CsPbI_2Br$ -based perovskite solar cells performance improvement.

4.5. $CsPbI_2Br$ -Based ($x=1$) and $CsPbI_{1.5}Br_{1.5}$ -Based ($x=1.5$) Perovskite Solar Cells

Figure 19a presents the loss comparison for $CsPbI_2Br$ -based perovskite solar cells including one data point for a $CsPbI_{1.5}Br_{1.5}$ PSC prepared by Zhang et al. Compared with most of $CsPbI_2Br$ -based perovskite solar cells, device from Zhang et al. exhibited satisfying balance between voltage and current losses, with $\Delta V_{oc}^{nonrad} = 280.5$ mV and $J_{sc}/J_{sc}^{SQ} = 90.3\%$.^[106] However, it seems hard to make a balance between voltage and current losses for most $CsPbI_2Br$ -based perovskite solar cells. To be specific, Yang et al.,^[130] Liang et al.,^[129] and Li et al.^[123] have achieved low ΔV_{oc}^{nonrad} , while the optimal J_{sc}/J_{sc}^{SQ} value among them was just 81.2%. Noted that all of them have adopted regulation process to narrow bandgaps and in consequence broadens the response range of external quantum efficiency and improves short-circuit current density J_{sc} and the power conversion efficiency η . It is surprising that such regulation could obtain lower ΔV_{oc}^{nonrad} than the others, rather than higher J_{sc}/J_{sc}^{SQ} value.

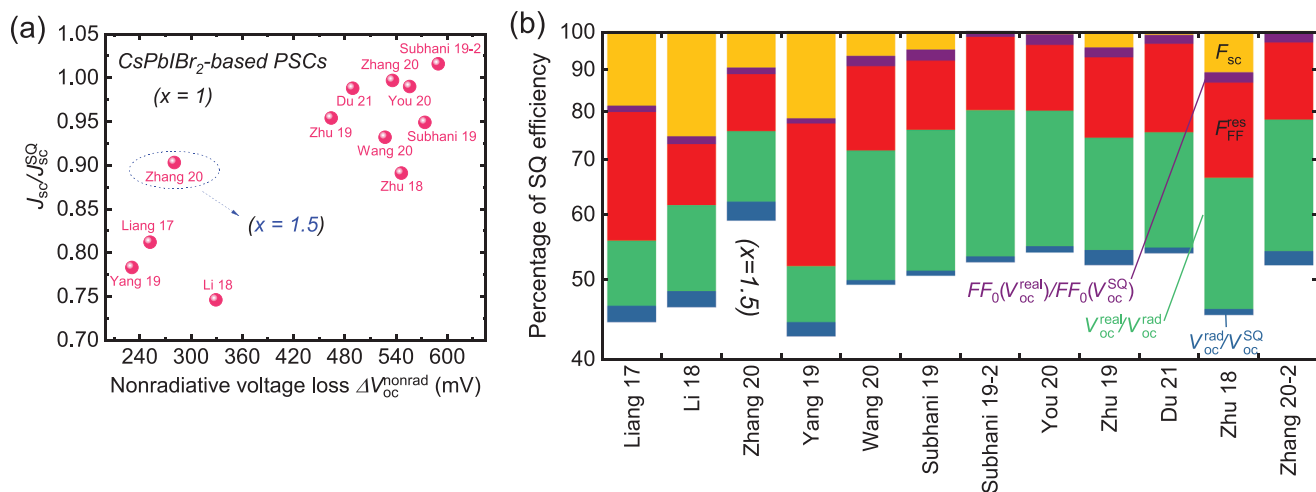


Figure 19. Loss comparison of $CsPbI_2Br$ -based ($x=1$) and $CsPbI_{1.5}Br_{1.5}$ -based ($x=1.5$) perovskite solar cells. a) Comparison of the J_{sc}/J_{sc}^{SQ} limitation with respect to nonradiative voltage ΔV_{oc}^{nonrad} . b) Visualization of potential improvement using FoMs of the efficiency losses. Devices are sorted from left to right by bandgap size.

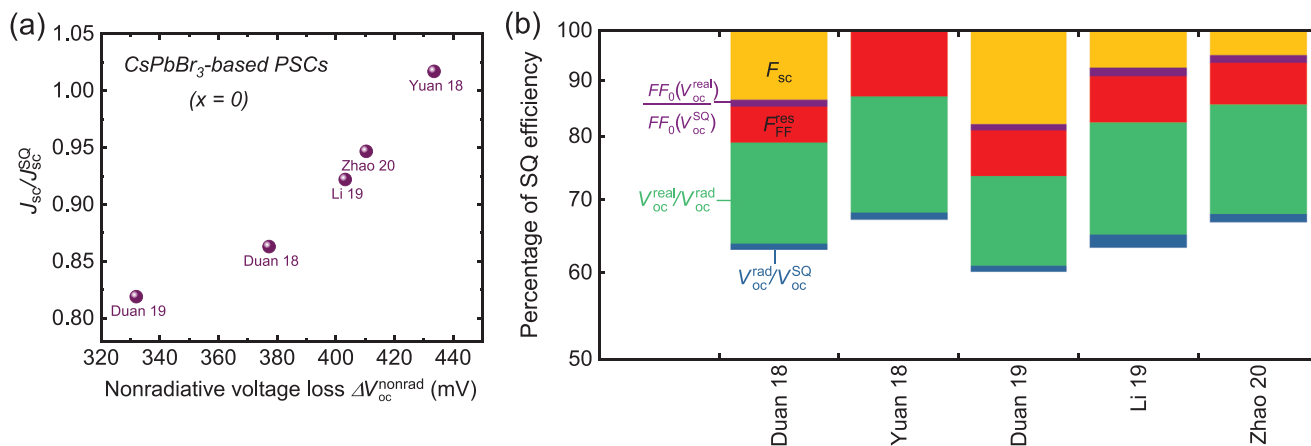


Figure 20. Loss comparison of CsPbBr₃-based perovskite solar cells. a) Comparison of the J_{sc}/J_{sc}^{SQ} limitation with respect to nonradiative voltage ΔV_{oc}^{nonrad} . b) Visualization of potential improvement using FoMs of the efficiency losses.

That means, though the range of external quantum efficiency has been broadened, more efforts are needed to effectively convert them into current and thus improve the ratio of J_{sc}/J_{sc}^{SQ} . On the contrary, for the others devices, which possess bandgap close to the intrinsic value (≈ 2.1 eV), they exhibit opposite situations. Namely, these devices show high J_{sc}/J_{sc}^{SQ} value as well as large ΔV_{oc}^{nonrad} , indicating that nonradiative recombination loss is the primary factor limiting device performance in this group. Noted that some devices exhibit ultrahigh J_{sc}/J_{sc}^{SQ} value of approximately 1. They will be discussed later. As shown in Figure 19b, the FoM of $V_{oc}^{real}/V_{oc}^{rad}$ dominates the energy losses overall, following by F_{FF}^{res} . For the devices from Yang et al.,^[130] Liang et al.,^[129] and Li et al.^[123] with smaller bandgaps, despite the effect of $V_{oc}^{real}/V_{oc}^{rad}$ has been reduced at a certain extent, the loss caused by F_{sc} increase significantly. For the CsPbI_{1.5}Br_{1.5} device reported by Zhang et al.,^[106] it presented lower loss overall, and the $V_{oc}^{real}/V_{oc}^{rad}$ is the dominated factor. It is noted that the devices shown in Figure 19b have been arranged depending on bandgap energy from small to large. We conclude that the main factor affecting energy losses changes from F_{sc} to $V_{oc}^{real}/V_{oc}^{rad}$ along with increasing bandgap energy, suggesting that targeted optimization approach should be performed. In addition, the F_{FF}^{res} occupied large percentage for all devices, indicating that series resistance reduction and ideality factor improvement are needed as well.

4.6. CsPbBr₃-Based (x = 0) Perovskite Solar Cells

Figure 20a presents the comparison of losses for CsPbBr₃-based perovskite solar cells. It can be seen that severe nonradiative recombination loss should be considered as the main factor limiting performance improvement. The lowest ΔV_{oc}^{nonrad} in this group is still as high as 332 mV.^[60] The other devices exhibit more severe nonradiative recombination loss,^[58,59,61] which is consistent with FoMs loss analysis shown in Figure 20b. Obviously, the green bar, which is related to $V_{oc}^{real}/V_{oc}^{rad}$ representing nonradiative recombination loss, is the largest. Note that Yuan et al.^[59] have fabricated solar cells with the structure

FTO/c-TiO₂/m-TiO₂/CsPb_{0.97}Tb_{0.03}Br₃/SnS:ZnS/NiO_x/carbon, leading to an ultrahigh J_{sc}/J_{sc}^{SQ} value beyond 1 leading to the disappearance of the bar for F_{sc} in Figure 20b.

4.7. Effect of J_{sc} Reporting Method on the Performance Loss Analysis

In the process of meta-analysis, we have found that many devices show ultrahigh J_{sc}/J_{sc}^{SQ} values, i.e., ultralow F_{sc} loss in the FoMs loss analysis figures. This phenomenon is usually observed for the CsPbI_xBr_{3-x} perovskite solar cells with small x value which have a relatively wide bandgap. We hold the opinion that such ultralow F_{sc} loss should be considered with caution. Almost all the stated J_{sc} (denote as J_{sc}^{sta}) are from the champion devices measured by the J - V measurement system with a standard solar simulator. These J_{sc}^{sta} values are usually higher than the average J_{sc} and the integrated value from the EQE (denote as J_{sc}^{EQE}). When the J_{sc}^{sta} strongly disagree with the J_{sc}^{EQE} , the J_{sc}^{sta}/J_{sc}^{SQ} will be significantly higher. This problem was overlooked for perovskite solar cells with narrow bandgap because they possess relatively high real J_{sc} , and thus the difference between J_{sc} and J_{sc}^{EQE} would not significantly affect the results. However, for perovskite solar cells with high E_g , it will result in the ultrahigh J_{sc}/J_{sc}^{SQ} value and ultralow F_{sc} loss.

For the need of parallel comparison, we still adopt the J_{sc}^{sta} from champion devices reported in the literature, because this is the most commonly used J_{sc} reporting method. Although it would underestimate the impact of F_{sc} , it can well reflect the differences between different devices and technology processes. In order to make the loss analysis more rigorous, we further discuss the perovskite solar cells with F_{sc} loss lower than 5% ($J_{sc}/J_{sc}^{SQ} > 95\%$) in Supporting Information (Section 6). We have compared the effects of J_{sc}^{sta} and J_{sc}^{EQE} on the performance loss distribution, as shown in Figure S17 and S18. The results show that the J_{sc} calculation method have significant influence on the F_{sc} loss but little influence on $V_{oc}^{real}/V_{oc}^{rad}$, V_{oc}^{rad}/V_{oc}^{SQ} , $FF_0(V_{oc}^{real})/FF_0(V_{oc}^{SQ})$ and F_{FF}^{res} . Hence, the results of these losses are still reliable in this situation. And the F_{sc} losses calculated by J_{sc}^{EQE}

are usually much higher than the losses calculated by J_{sc}^{sta} . Considering the measurement process of J_{sc}^{sta} and J_{sc}^{EQE} , we believe that the real F_{sc} loss should be somewhere in between. Finally, although many research groups have begun to pay attention to the report of J_{sc} and presented several different measurement results in their papers, we still call on people to treat the report of J_{sc} more strictly, especially for the perovskite solar cells with high E_g . Due to the presence of deviation in preparation and measurement process, the performances of champion devices are likely to be unreliable when J_{sc}/J_{sc}^{SQ} values approach or even exceeds 1, but other performance metrics are not good enough.

5. Conclusions and Outlook

We have performed a detailed meta-analysis of key performance parameters of all-inorganic $CsPbI_xBr_{3-x}$ ($0 \leq x \leq 3$) perovskite-based solar cells and absorber materials. Given that all-inorganic perovskites cover a wide range of bandgaps that go up to values of 2.3 eV, i.e., much higher than ideal for single junction solar cells, it is imperative to correct device performance data for the influence of bandgap. Therefore, we used a consistent way of determining the bandgap from the inflection point of the quantum efficiency that is in line with other efforts such as the emerging-PV project.^[7] Using the bandgap, we determined performance parameters in the SQ model and referenced all experimental data to the respective values in the SQ model. From this data and meta-analyses of the material parameters such as mobility and photoluminescence lifetime, we can make conclusions on the whole material family as well as obtain more detailed insights as a function of stoichiometry. Independent of the I to Br ratio, $CsPbI_xBr_{3-x}$ perovskite layers show similar carrier mobilities as compared to hybrid lead-halide perovskites but so far shorter photoluminescence lifetimes and lower external photoluminescence quantum efficiencies. Thus, all-inorganic perovskite solar cells have more severe nonradiative recombination losses over the whole range of bandgaps, and hence lower V_{oc}/V_{oc}^{SQ} and η/η^{SQ} ratios in devices as compared to hybrid perovskites. However, we also note that given the current level of work (measured in the accumulated number of publications) invested into the material system, all-inorganic perovskite solar cells don't perform worse than hybrid ones at a similar stage in their development.

While V_{oc} losses are the largest fraction of the total losses for basically all studied devices, fill factor losses are also quite substantial in particular in case of higher-bandgap perovskites. This suggests that tackling resistive limitations is important for a further improvement of efficiencies. Photocurrent losses are overall the least significant in most of the devices that are best of their respective bandgap range. While this is generally a good sign and an indication of a high absorption coefficient and sufficient mobilities of absorber and contact layers, we note that the losses get significantly lower with higher bandgap with some of the cells having values above the SQ model. While this is not technically impossible given the definition of the bandgap via the inflection point, those cells often have discrepancies between the current densities derived from quantum efficiency measurements and the current densities derived from current-voltage

curves. This suggests that at least some of the values might be affected by calibration issues. A further trend seen as a function of bandgap is a decrease of PL lifetime of films with increasing bandgap. This trend is consistent with the trend in non-radiative recombination losses in full devices. Here, we note that in both cases, the $CsPbIBr_2$ -based devices break the trend as they show even higher voltage losses and lower lifetimes than the higher-bandgap $CsPbBr_3$ -based samples. Achieving an improved balance between voltage and photocurrent losses is another key requirement for better performance. Our meta-analysis shows a trade-off between these two factors. The lowest ΔV_{oc}^{nonrad} of 116 mV is achieved by lower E_g $CsPbI_3$ devices, while only achieving 84.4% of J_{sc}/J_{sc}^{SQ} . On the contrary, for the higher E_g $CsPbBr_3$ and $CsPbIBr_2$ devices with $J_{sc}/J_{sc}^{SQ} > 95\%$, the ΔV_{oc}^{nonrad} loss increases to over 400 mV.

Finally, we also performed a meta-analysis of the used contact layers. Given the higher annealing temperatures, all-inorganic perovskites are mostly prepared in the structure that is often called the regular structure and that starts the deposition with an ETL that is normally a metal oxide (TiO_2 or SnO_2) that can withstand the required higher annealing temperatures much better than the organic HTLs that are typically used for inverted geometries. Here, we want to point out that there is over all rather little variation in the used contact layers, with Spiro-OMeTAD dominating the used HTLs over the whole range of I to Br ratios. However, given the large range of bandgaps covered, it is likely that perfect (or even good) band alignment can only be achieved by a tiny subsection of the studied compositions while many of the layer stacks may suffer from additional recombination losses at interfaces. As TiO_2/SnO_2 and Spiro-OMeTAD have been shown to be compatible with high-efficiency lower-bandgap hybrid perovskites,^[138,141] it is likely that especially the higher-bandgap all-inorganic perovskite solar cells suffer from this effect.

To achieve a higher degree of technological maturity and improved device performance in all inorganic perovskites, understanding of carrier recombination processes in the bulk and at the interfaces is essential. All-inorganic perovskites have shorter photoluminescence lifetimes and lower photoluminescence quantum efficiencies than the best hybrid lead-halide perovskites. While there are already many experimental studies on the topic, theoretical work on the dominant defects and their impact on the recombination rates and lifetimes is so far relatively scarce. We think theoretical work, identifying the dominant defects and their associated capture coefficients and formation energies would be highly valuable.^[87] If we know the dominant defect species, we can adjust processing conditions to eliminate the source of defect formation. An example for a such a change in processing conditions could be, e.g., a change in the ratio of precursors to achieve a stoichiometry that has an excess of a certain element which is harmful as a vacancy. Furthermore, changes in stoichiometry can also lead to changes in formation energies of defects and may therefore be a feasible way to reduce the densities of certain defects. In addition, calculated capture coefficients are often (but not always) fairly different for electrons and holes (see Figure 6).^[87] Assuming for instance that the electron capture rate is much slower than the hole capture rate, the entire recombination process would be rate limited by electron capture. Thus, if one was able to further

slow down electron capture, the whole process could be further slowed down and efficiency would increase. Such a slowing down of the rate could be achieved by reducing the density of (in this example) electrons, e.g. by introducing doping or by adjusting the properties of the electron injecting contacts relative to the hole injecting contacts such that one type of carrier is present in excess of the other.^[101]

Another major aspect that will help direct process and device optimization will be to develop a suitable set of characterization methods to identify the dominant efficiency limiting mechanisms in all-inorganic but also in hybrid perovskites. The determination of many key parameters such as defect densities, recombination lifetimes or the efficiency of charge extraction that are necessary for improving our understanding of charge-carrier recombination could be improved. So far, defect densities are frequently measured using the trap-filled regime in single carrier devices, which is highly problematic due to electrostatic limitations^[96] of the method and the dangers associated with neglecting the influence of injection barriers^[142] and moving ions.^[94,143] Steady-state and transient photoluminescence are frequently used to study recombination. However, often also information about charge extraction or charge collection are derived from photoluminescence. For instance, the quenching of the steady-state photoluminescence when attaching electron- or hole-transport layers is often considered a way of identifying efficient charge extraction.^[144–146] However, in fact this only clarifies that the electron- or hole-transport layer will increase charge recombination and is hence a clearly negative factor that should correlate with losses in open-circuit voltage. A better way of extracting information on charge collection from photoluminescence is to compare PL at short circuit and open circuit^[144] or to even measure voltage-dependent photoluminescence in complete devices.^[145] Furthermore, it may be possible to develop new experimental methods sensitive to charge extraction and collection based, e.g., on the rise of the photovoltage in different transient methods.^[146] Thus, we hope that the technological development of all inorganic perovskite solar cells will be enabled and accompanied by improvements in theoretical understanding and characterization of efficiency limiting processes.

Supporting Information

Supporting Information is available from the Wiley Online Library or from the author.

Acknowledgements

Y.Y. and G.Y. thank the financial support by China and Germany Postdoctoral Exchange Program. T.K. acknowledges funding by the Helmholtz Association. The authors declare no competing interest.

Open access funding enabled and organized by Projekt DEAL.

Conflict of Interest

The authors declare no conflict of interest.

Keywords

all-inorganic perovskite solar cells, material properties, performance loss analysis, Shockley–Queisser limit

Received: October 11, 2021

Revised: December 22, 2021

Published online: March 28, 2022

- [1] S. De Wolf, J. Holovsky, S.-J. Moon, P. Löper, B. Niesen, M. Ledinsky, F.-J. Haug, J.-H. Yum, C. Ballif, *J. Phys. Chem. Lett.* **2014**, 5, 1035.
- [2] T. Leijtens, K. A. Bush, R. Prasanna, M. D. McGehee, *Nat. Energy* **2018**, 3, 828.
- [3] S. Essig, C. Allebé, T. Remo, J. F. Geisz, M. A. Steiner, K. Horowitz, L. Barraud, J. S. Ward, M. Schnabel, A. Descoeudres, David L. Young, M. Woodhouse, M. Despeisse, C. Ballif, A. Tamboli, *Nat. Energy* **2017**, 2, 17144.
- [4] M. A. Green, A. Ho-Baillie, H. J. Snaith, *Nat. Photonics* **2014**, 8, 506.
- [5] M. A. Green, A. W. Y. Ho-Baillie, *ACS Energy Lett.* **2019**, 4, 1639.
- [6] J. F. Guillemoles, T. Kirchartz, D. Cahen, U. Rau, *Nat. Photonics* **2019**, 13, 501.
- [7] O. Almora, D. Baran, G. C. Bazan, C. Berger, C. I. Cabrera, K. R. Catchpole, S. Erten-Ela, F. Guo, J. Hauch, A. W. Y. Ho-Baillie, T. J. Jacobsson, R. A. J. Janssen, T. Kirchartz, N. Kopidakis, Y. Li, M. A. Loi, R. R. Lunt, X. Mathew, M. D. McGehee, J. Min, D. B. Mitzi, M. K. Nazeeruddin, J. Nelson, A. F. Nogueira, U. W. Paetzold, N.-G. Park, B. P. Rand, U. Rau, H. J. Snaith, E. Unger, et al., *Adv. Energy Mater.* **2021**, 11, 2002774.
- [8] R. Brenes, D. Guo, A. Osherov, N. K. Noel, C. Eames, E. M. Hutter, S. K. Pathak, F. Niroui, R. H. Friend, M. S. Islam, H. J. Snaith, V. Bulović, T. J. Savenije, S. D. Stranks, *Joule* **2017**, 1, 155.
- [9] M. H. Du, *J. Phys. Chem. Lett.* **2015**, 6, 1461.
- [10] R. E. Brandt, J. R. Poindexter, P. Gorai, R. C. Kurchin, R. L. Z. Hoye, L. Nienhaus, M. W. B. Wilson, J. A. Polizzotti, R. Sereika, R. Zaltauskas, L. C. Lee, J. L. MacManus-Driscoll, M. Bawendi, V. Stevanović, T. Buonassisi, *Chem. Mater.* **2017**, 29, 4667.
- [11] R. E. Brandt, V. Stevanović, D. S. Ginley, T. Buonassisi, *MRS Commun.* **2015**, 5, 265.
- [12] Y. Rong, Y. Hu, A. Mei, H. Tan, M. I. Saidaminov, S. I. Seok, M. D. McGehee, E. H. Sargent, H. Han, *Science* **2018**, 361, eaat8235.
- [13] a) S. Y. Park, J.-S. Park, B. J. Kim, H. Lee, A. Walsh, K. Zhu, D. H. Kim, H. S. Jung, *Nat. Sustainability* **2020**, 3, 1044; b) K. P. Goetz, A. D. Taylor, Y. J. Hofstetter, Y. Vaynzof, *ACS Appl. Mater. Interfaces* **2021**, 13, 1; c) S. Chen, Y. Deng, X. Xiao, S. Xu, P. N. Rudd, J. Huang, *Nat. Sustainability* **2021**, 4, 636; d) S. Chen, Y. Deng, H. Gu, S. Xu, S. Wang, Z. Yu, V. Blum, J. Huang, *Nat. Energy* **2020**, 5, 1003; e) L. Shi, M. P. Bucknall, T. L. Young, M. Zhang, L. Hu, J. Bing, D. S. Lee, J. Kim, T. Wu, N. Takamure, D. R. McKenzie, S. Huang, M. A. Green, A. W. Y. Ho-Baillie, *Science* **2020**, 368, eaba2412; f) X. Li, F. Zhang, H. He, J. J. Berry, K. Zhu, T. Xu, *Nature* **2020**, 578, 555.
- [14] A. F. Akbulatov, V. M. Martynenko, L. A. Frolova, N. N. Dremova, I. Zhidkov, S. A. Tsarev, S. Y. Luchkin, E. Z. Kurmaev, S. M. Aldoshin, K. J. Stevenson, P. A. Troshin, *Sol. Energy Mater. Sol. Cells* **2020**, 213, 110559.
- [15] V. M. Goldschmidt, *Naturwissenschaften* **1926**, 14, 477.
- [16] X. Liu, R. Hong, C. Tian, *J. Mater. Sci.: Mater. Electron.* **2008**, 20, 323.
- [17] G. Kieslich, S. J. Sun, A. K. Cheetham, *Chem. Sci.* **2014**, 5, 4712.
- [18] a) M. Saliba, T. Matsui, J.-Y. Seo, K. Domanski, J.-P. Correa-Baena, M. K. Nazeeruddin, S. M. Zakeeruddin, W. Tress, A. Abate,

- A. Hagfeldt, M. Grätzel, *Energy Environ. Sci.* **2016**, 9, 1989;
- b) J.-W. Lee, D.-H. Kim, H.-S. Kim, S.-W. Seo, S. M. Cho, N.-G. Park, *Adv. Energy Mater.* **2015**, 5, 1501310; c) M. Saliba, T. Matsui, K. Domanski, J.-Y. Seo, A. Ummadisingu, S. M. Zakeeruddin, J.-P. Correa-Baena, W. R. Tress, A. Abate, A. Hagfeldt, M. Grätzel, *Science* **2016**, 354, 206; d) X. Zheng, Y. Hou, C. Bao, J. Yin, F. Yuan, Z. Huang, K. Song, J. Liu, J. Troughton, N. Gasparini, C. Zhou, Y. Lin, D.-J. Xue, B. Chen, A. K. Johnston, N. Wei, M. N. Hedhili, M. Wei, A. Y. Alsalloum, P. Maity, B. Turedi, C. Yang, D. Baran, T. D. Anthopoulos, Y. Han, Z.-H. Lu, O. F. Mohammed, F. Gao, E. H. Sargent, O. M. Bakr, *Nat. Energy* **2020**, 5, 131; e) P. Zhao, B. J. Kim, X. Ren, D. G. Lee, G. J. Bang, J. B. Jeon, W. B. Kim, H. S. Jung, *Adv. Mater.* **2018**, 30, 1802763.
- [19] Q. Ye, Y. Zhao, S. Mu, P. Gao, X. Zhang, J. You, *Sci. China: Chem.* **2019**, 62, 810.
- [20] J. J. Tian, Q. F. Xue, Q. Yao, N. Li, C. J. Brabec, H. L. Yip, *Adv. Energy Mater.* **2020**, 10, 2000183.
- [21] G. Kieslich, S. Sun, A. K. Cheetham, *Chem. Sci.* **2014**, 5, 4712.
- [22] Z. Chen, J. J. Wang, Y. Ren, C. Yu, K. Shum, *Appl. Phys. Lett.* **2012**, 101, 093901.
- [23] A. Swarnkar, A. R. Marshall, E. M. Sanehira, B. D. Chernomordik, D. T. Moore, J. A. Christians, T. Chakrabarti, J. M. Luther, *Science* **2016**, 354, 92.
- [24] H. Choi, J. Jeong, H.-B. Kim, S. Kim, B. Walker, G.-H. Kim, J. Y. Kim, *Nano Energy* **2014**, 7, 80.
- [25] S. M. Yoon, H. Min, J. B. Kim, G. Kim, K. S. Lee, S. I. Seok, *Joule* **2021**, 5, 183.
- [26] Y. Wang, M. I. Dar, L. K. Ono, T. Y. Zhang, M. Kan, Y. W. Li, L. J. Zhang, X. T. Wang, Y. G. Yang, X. Y. Gao, Y. B. Qi, M. Grätzel, Y. X. Zhao, *Science* **2019**, 365, 591.
- [27] W. Shockley, H. J. Queisser, *J. Appl. Phys.* **1961**, 32, 510.
- [28] K. Wang, C. Gao, Z. Xu, Q. Tian, X. Gu, L. Zhang, S. Zhang, K. Zhao, S. Liu, *Adv. Funct. Mater.* **2021**, 31, 2101568.
- [29] Z. Guo, A. K. Jena, I. Takei, M. Ikegami, A. Ishii, Y. Numata, N. Shibayama, T. Miyasaka, *Adv. Funct. Mater.* **2021**, 31, 2103614.
- [30] B. W. Gao, J. Meng, *ACS Appl. Energy Mater.* **2020**, 3, 8249.
- [31] J. L. Duan, Y. D. Wang, X. Y. Yang, Q. W. Tang, *Angew. Chem., Int. Ed.* **2020**, 59, 4391.
- [32] National Renewable Energy Laboratory (NREL), Best Research-Cell Efficiency Chart, <https://www.nrel.gov/pv/cell-efficiency.html> (accessed: April 2021).
- [33] M. Green, E. Dunlop, J. Hohl-Ebinger, M. Yoshita, N. Kopidakis, X. Hao, *Prog. Photovoltaics* **2021**, 29, 3.
- [34] P. Kaienburg, L. Krückemeier, D. Lübke, J. Nelson, U. Rau, T. Kirchartz, *Phys. Rev. Res.* **2020**, 2, 023109.
- [35] a) J. H. Noh, S. H. Im, J. H. Heo, T. N. Mandal, S. I. Seok, *Nano Lett.* **2013**, 13, 1764; b) B. Slimi, M. Mollar, I. Ben Assaker, A. Kriaa, R. Chtourou, B. Mari, *Monatsh. Chem.* **2017**, 148, 835.
- [36] Y. Wang, T. Y. Zhang, M. Kan, Y. X. Zhao, *J. Am. Chem. Soc.* **2018**, 140, 12345.
- [37] Y. Wang, X. M. Liu, T. Y. Zhang, X. T. Wang, M. Kan, J. L. Shi, Y. X. Zhao, *Angew. Chem., Int. Ed.* **2019**, 58, 16691.
- [38] Q. Ye, F. Ma, Y. Zhao, S. Yu, Z. Chu, P. Gao, X. Zhang, J. You, *Small* **2020**, 16, 2005246.
- [39] X. M. Chang, J. J. Fang, Y. Y. Fan, T. Luo, H. Su, Y. L. Zhang, J. Lu, L. Tsetseris, T. D. Anthopoulos, S. Z. Liu, K. Zhao, *Adv. Mater.* **2020**, 32, 2001243.
- [40] T. T. Liu, J. Zhang, M. C. Qin, X. Wu, F. Z. Li, X. H. Lu, Z. L. Zhu, A. K.-Y. Jen, *Adv. Funct. Mater.* **2021**, 31, 2009515.
- [41] B. Yu, J. Shi, S. Tan, Y. Cui, W. Zhao, H. Wu, Y. Luo, D. Li, Q. Meng, *Angew. Chem., Int. Ed.* **2021**, 60, 13436.
- [42] W. J. Chen, H. Y. Chen, G. Y. Xu, R. M. Xue, S. H. Wang, Y. W. Li, Y. F. Li, *Joule* **2019**, 3, 304.
- [43] K. L. Wang, R. Wang, Z. K. Wang, M. Li, Y. Zhang, H. Ma, L. S. Liao, Y. Yang, *Nano Lett.* **2019**, 19, 5176.
- [44] J. J. Tian, Q. F. Xue, X. F. Tang, Y. X. Chen, N. Li, Z. C. Hu, T. T. Shi, X. Wang, F. Huang, C. J. Brabec, H. L. Yip, Y. Cao, *Adv. Mater.* **2019**, 31, 1901152.
- [45] E. C. Shen, J. D. Chen, Y. Tian, Y. X. Luo, Y. Shen, Q. Sun, T. Y. Jin, G. Z. Shi, Y. Q. Li, J. X. Tang, *Adv. Sci.* **2020**, 7, 9.
- [46] J. V. Patil, S. S. Mali, C. K. Hong, *ACS Appl. Mater. Interfaces* **2020**, 12, 27176.
- [47] J. V. Patil, S. S. Mali, C. K. Hong, *Sol. RRL* **2020**, 4, 2000164.
- [48] Y. X. Luo, J. D. Chen, H. Y. Hou, Y. C. Ye, K. C. Shen, L. Y. Lu, Y. Q. Li, F. Song, X. Y. Gao, J. X. Tang, *ACS Appl. Mater. Interfaces* **2020**, 12, 41596.
- [49] P. Wang, H. Wang, Y. C. Mao, H. J. Zhang, F. H. Ye, D. Liu, T. Wang, *Adv. Sci.* **2020**, 7, 2000421.
- [50] Z. Guo, A. K. Jena, I. Takei, G. M. Kim, M. A. Kamarudin, Y. Sanehira, A. Ishii, Y. Numata, S. Hayase, T. Miyasaka, *J. Am. Chem. Soc.* **2020**, 142, 9725.
- [51] M. Wang, F. R. Cao, M. Wang, K. M. Deng, L. Li, *Adv. Mater.* **2021**, 33, 2006745.
- [52] W. D. Zhu, Q. N. Zhang, D. Z. Chen, Z. Y. Zhang, Z. H. Lin, J. J. Chang, J. C. Zhang, C. F. Zhang, Y. Hao, *Adv. Energy Mater.* **2018**, 8, 1802080.
- [53] W. S. Subhani, K. Wang, M. Y. Du, X. L. Wang, S. Z. Liu, *Adv. Energy Mater.* **2019**, 9, 1803785.
- [54] W. D. Zhu, Z. Y. Zhang, W. M. Chai, Q. N. Zhang, D. Z. Chen, Z. H. Lin, J. J. Chang, J. C. Zhang, C. F. Zhang, Y. Hao, *ChemSusChem* **2019**, 12, 2318.
- [55] W. H. Zhang, J. Xiong, J. H. Li, W. A. Daoud, *Small* **2020**, 16, 2001535.
- [56] Y. B. You, W. Tian, M. Wang, F. R. Cao, H. X. Sun, L. Li, *Adv. Mater. Interfaces* **2020**, 7, 9.
- [57] J. Du, J. L. Duan, X. Y. Yang, Y. Y. Duan, Q. Z. Zhou, Q. W. Tang, *Angew. Chem., Int. Ed.* **2021**, 60, 10608.
- [58] J. L. Duan, Y. Y. Zhao, X. Y. Yang, Y. D. Wang, B. L. He, Q. W. Tang, *Adv. Energy Mater.* **2018**, 8, 1802346.
- [59] H. W. Yuan, Y. Y. Zhao, J. L. Duan, Y. D. Wang, X. Y. Yang, Q. W. Tang, *J. Mater. Chem. A* **2018**, 6, 24324.
- [60] J. L. Duan, Y. Y. Zhao, Y. D. Wang, X. Y. Yang, Q. W. Tang, *Angew. Chem., Int. Ed.* **2019**, 58, 16147.
- [61] X. Li, Y. Tan, H. Lai, S. P. Li, Y. Chen, S. W. Li, P. Xu, J. Y. Yang, *ACS Appl. Mater. Interfaces* **2019**, 11, 29746.
- [62] Y. Y. Zhao, J. L. Duan, Y. D. Wang, X. Y. Yang, Q. W. Tang, *Nano Energy* **2020**, 67, 9.
- [63] M. Ledinsky, T. Šchönfeldová, J. Holovský, E. Aydin, Z. Hájková, L. Landová, N. Neyková, A. Fejfar, S. De Wolf, *J. Phys. Chem. Lett.* **2019**, 10, 1368.
- [64] T. C. M. Müller, T. Kirchartz, in *Advanced Characterization Techniques for Thin Film Solar Cells*, (Eds: D. Abou-Ras, T. Kirchartz, U. Rau), Wiley-VCH, Weinheim, Germany **2016**, p. 189.
- [65] U. Rau, B. Blank, T. C. M. Müller, T. Kirchartz, *Phys. Rev. Appl.* **2017**, 7, 044016.
- [66] a) E. M. Sanehira, A. R. Marshall, J. A. Christians, S. P. Harvey, P. N. Ciesielski, L. M. Wheeler, P. Schulz, L. Y. Lin, M. C. Beard, J. M. Luther, *Sci. Adv.* **2017**, 3, eaao4204; b) P. Becker, J. A. Marquez, J. Just, A. Al-Ashouri, C. Hages, H. Hempel, M. Jost, S. Albrecht, R. Frahm, T. Unold, *Adv. Energy Mater.* **2019**, 9, 1900555; c) C. Liu, Y. Yang, O. A. Syzgantseva, Y. Ding, M. A. Syzgantseva, X. Zhang, A. M. Asiri, S. Dai, M. K. Nazeeruddin, *Adv. Mater.* **2020**, 32, 2002632.
- [67] S. Dastidar, S. Li, S. Y. Smolin, J. B. Baxter, A. T. Fafarman, *ACS Energy Lett.* **2017**, 2, 2239.
- [68] Y. Meng, C. Y. Lan, F. Z. Li, S. Yip, R. J. Wei, X. L. Kang, X. M. Bu, R. T. Dong, H. Zhang, J. C. Ho, *ACS Nano* **2019**, 13, 6060.
- [69] H. Zhang, E. Debroye, J. A. Steele, M. B. J. Rooftaers, J. Hofkens, H. I. Wang, M. Bonn, *ACS Energy Lett.* **2021**, 6, 568.
- [70] C. L. Kennedy, A. H. Hill, E. S. Massaro, E. M. Grumstrup, *ACS Energy Lett.* **2017**, 2, 1501.

- [71] C. Liu, Y. Yang, C. Zhang, S. Wu, L. Wei, F. Guo, G. M. Arumugam, J. Hu, X. Liu, J. Lin, R. E. I. Schropp, Y. Mai, *Adv. Mater.* **2020**, *32*, 1907361.
- [72] a) X. Gong, L. Guan, Q. Li, Y. Li, T. Zhang, H. Pan, Q. Sun, Y. Shen, C. Graetzel, S. M. Zakeeruddin, M. Graetzel, M. Wang, *Sci. Adv.* **2020**, *6*, eaay5661; b) S. M. Yang, H. Zhao, M. Wu, S. H. Yuan, Y. Han, Z. K. Liu, K. P. Guo, S. Z. Liu, S. Yang, H. Zhao, S. Yuan, Y. Han, Z. Liu, S. Liu, M. Wu, K. Guo, *Sol. Energy Mater. Sol. Cells* **2019**, *201*, 110052; c) Z. Wang, J. Gan, X. Liu, H. Shi, Q. Wei, Q. Zeng, L. Qiao, Y. Zheng, *J. Power Sources* **2020**, *454*, 227913.
- [73] X. Y. Meng, Z. Wang, W. Qian, Z. L. Zhu, T. Zhang, Y. Bai, C. Hu, S. Xiao, Y. L. Yang, S. H. Yang, *J. Phys. Chem. Lett.* **2019**, *10*, 194.
- [74] a) Y. You, W. Tian, M. Wang, F. Cao, H. Sun, L. Li, *Adv. Mater. Interfaces* **2020**, *7*, 2000537; b) Q. N. Zhang, W. D. Zhu, D. Z. Chen, Z. Y. Zhang, Z. H. Lin, J. J. Chang, J. C. Zhang, C. F. Zhang, Y. Hao, *ACS Appl. Mater. Interfaces* **2019**, *11*, 2997; c) D. Wang, W. Li, R. Li, W. Sun, J. Wu, Z. Lan, *Sol. RRL* **2021**, *5*, 2100375; d) Y. Wang, K. Wang, W. S. Subhani, C. Zhang, X. Jiang, S. Wang, H. Bao, L. Liu, L. Wan, S. Liu, *Small* **2020**, *16*, 1907283; e) Q. Zhang, W. Zhu, D. Chen, Z. Zhang, Z. Lin, J. Chang, J. Zhang, C. Zhang, Y. Hao, *ACS Appl. Mater. Interfaces* **2019**, *11*, 2997; f) J. Lu, S.-C. Chen, Q. Zheng, *ACS Appl. Energy Mater.* **2018**, *1*, 5872; g) J. Yang, Q. Zhang, J. Xu, H. Liu, R. Qin, H. Zhai, S. Chen, M. Yuan, *Nanomaterials* **2019**, *9*, 1666.
- [75] a) B. Yang, F. Zhang, J. Chen, S. Yang, X. Xia, T. Pullerits, W. Deng, K. Han, *Adv. Mater.* **2017**, *29*, 1703758; b) C. C. Stoumpos, C. D. Malliakas, J. A. Peters, Z. Liu, M. Sebastian, J. Im, T. C. Chasapis, A. C. Wibowo, D. Y. Chung, A. J. Freeman, B. W. Wessels, M. G. Kanatzidis, *Cryst. Growth Des.* **2013**, *13*, 2722; c) J. Chen, D. J. Morrow, Y. Fu, W. Zheng, Y. Zhao, L. Dang, M. J. Stolt, D. D. Kohler, X. Wang, K. J. Czech, M. P. Hautzinger, S. Shen, L. Guo, A. Pan, J. C. Wright, S. Jin, *J. Am. Chem. Soc.* **2017**, *139*, 13525.
- [76] H. Zhu, M. T. Trinh, J. Wang, Y. Fu, P. P. Joshi, K. Miyata, S. Jin, X.-Y. Zhu, *Adv. Mater.* **2017**, *29*, 1603072.
- [77] J. Z. Song, Q. Z. Cui, J. H. Li, J. Y. Xu, Y. Wang, L. M. Xu, J. Xue, Y. H. Dong, T. Tian, H. D. Sun, H. B. Zeng, *Adv. Opt. Mater.* **2017**, *5*, 1700157.
- [78] a) C. X. Huo, X. H. Liu, X. F. Song, Z. M. Wang, H. B. Zeng, *J. Phys. Chem. Lett.* **2017**, *8*, 4785; b) J. P. Zeng, X. M. Li, Y. Wu, D. D. Yang, Z. G. Sun, Z. H. Song, H. Wang, H. B. Zeng, *Adv. Funct. Mater.* **2018**, *28*, 1804394; c) J. Kim, L. Hu, H. J. Chen, X. W. Guan, P. R. Anandan, F. Li, J. B. Tang, C. H. Lin, K. Kalantar-Zadeh, A. Tricoli, T. Wu, *ACS Mater. Lett.* **2020**, *2*, 1368; d) Z. Yang, M. Q. Wang, H. W. Qiu, X. Yao, X. Z. Lao, S. J. Xu, Z. H. Lin, L. Y. Sun, J. Y. Shao, *Adv. Funct. Mater.* **2018**, *28*, 1705908; e) M. I. Saidaminov, M. A. Haque, J. Almutlaq, S. Sarmah, X. H. Miao, R. Begum, A. A. Zhumekenov, I. Dursun, N. Cho, B. Murali, O. F. Mohammed, T. Wu, O. M. Bakr, *Adv. Opt. Mater.* **2017**, *5*, 1600704; f) X. Hu, X. Wang, P. Fan, Y. Li, X. Zhang, Q. Liu, W. Zheng, G. Xu, X. Wang, X. Zhu, A. Pan, *Nano Lett.* **2018**, *18*, 3024.
- [79] a) G. E. Eperon, S. D. Stranks, C. Menelaou, M. B. Johnston, L. M. Herz, H. J. Snaith, *Energy Environ. Sci.* **2014**, *7*, 982; b) W. Rehman, R. L. Milot, G. E. Eperon, C. Wehrenfennig, J. L. Boland, H. J. Snaith, M. B. Johnston, L. M. Herz, *Adv. Mater.* **2015**, *27*, 7938; c) A. A. Zhumekenov, M. I. Saidaminov, M. A. Haque, E. Alarousu, S. P. Sarmah, B. Murali, I. Dursun, X.-H. Miao, A. L. Abdelhady, T. Wu, O. F. Mohammed, O. M. Bakr, *ACS Energy Lett.* **2016**, *1*, 32; d) Q. Han, S.-H. Bae, P. Sun, Y.-T. Hsieh, Y. Yang, Y. S. Rim, H. Zhao, Q. Chen, W. Shi, G. Li, Y. Yang, *Adv. Mater.* **2016**, *28*, 2253; e) D. H. Kim, J. Park, Z. Li, M. J. Yang, J. S. Park, I. J. Park, J. Y. Kim, J. J. Berry, G. Rumbles, K. Zhu, *Adv. Mater.* **2017**, *29*, 1606831.
- [80] a) S. D. Stranks, G. E. Eperon, G. Grancini, C. Menelaou, M. J. P. Alcocer, T. Leijtens, L. M. Herz, A. Petrozza, H. J. Snaith, *Science* **2013**, *342*, 341; b) G. Xing, N. Mathews, S. Sun, S. S. Lim, Y. M. Lam, M. Grätzel, S. Mhaisalkar, T. C. Sum, *Science* **2013**, *342*, 344; c) Z. Guo, J. S. Manser, Y. Wan, P. V. Kamat, L. Huang, *Nat. Commun.* **2015**, *6*, 7471; d) C. S. Ponseca, T. J. Savenije, M. Abdellah, K. Zheng, A. Yartsev, T. Pascher, T. Harlang, P. Chabera, T. Pullerits, A. Stepanov, J.-P. Wolf, V. Sundström, *J. Am. Chem. Soc.* **2014**, *136*, 5189; e) C. La-o-vorakiat, T. Salim, J. Kadro, M.-T. Khuc, R. Haselsberger, L. Cheng, H. Xia, G. G. Gurzadyan, H. Su, Y. M. Lam, R. A. Marcus, M.-E. Michel-Beyerle, E. E. M. Chia, *Nat. Commun.* **2015**, *6*, 7903; f) E. M. Hutter, G. E. Eperon, S. D. Stranks, T. J. Savenije, *J. Phys. Chem. Lett.* **2015**, *6*, 3082; g) O. G. Reid, M. Yang, N. Kopidakis, K. Zhu, G. Rumbles, *ACS Energy Lett.* **2016**, *1*, 561; h) D. H. Kim, J. Park, Z. Li, M. Yang, J.-S. Park, I. J. Park, J. Y. Kim, J. J. Berry, G. Rumbles, K. Zhu, *Adv. Mater.* **2017**, *29*, 1606831; i) D. A. Valverde-Chávez, C. S. Ponseca, C. C. Stoumpos, A. Yartsev, M. G. Kanatzidis, V. Sundström, D. G. Cooke, *Energy Environ. Sci.* **2015**, *8*, 3700; j) O. E. Semonin, G. A. Elbaz, D. B. Straus, T. D. Hull, D. W. Paley, A. M. van der Zande, J. C. Hone, I. Kymissis, C. R. Kagan, X. Roy, J. S. Owen, *J. Phys. Chem. Lett.* **2016**, *7*, 3510; k) Q. Dong, Y. Fang, Y. Shao, P. Mulligan, J. Qiu, L. Cao, J. Huang, *Science* **2015**, *347*, 967; l) M. I. Saidaminov, A. L. Abdelhady, B. Murali, E. Alarousu, V. M. Burlakov, W. Peng, I. Dursun, L. Wang, Y. He, G. Maculan, A. Goriely, T. Wu, O. F. Mohammed, O. M. Bakr, *Nat. Commun.* **2015**, *6*, 7586; m) D. Shi, V. Adinolfi, R. Comin, M. Yuan, E. Alarousu, A. Buin, Y. Chen, S. Hoogland, A. Rothenberger, K. Katsiev, Y. Losovyj, X. Zhang, P. A. Dowben, O. F. Mohammed, E. H. Sargent, O. M. Bakr, *Science* **2015**, *347*, 519; n) O. Gunawan, S. R. Pae, D. M. Bishop, Y. Virgus, J. H. Noh, N. J. Jeon, Y. S. Lee, X. Y. Shao, T. Todorov, D. B. Mitzi, B. Shin, *Nature* **2019**, *575*, 151.
- [81] R. L. Milot, G. E. Eperon, H. J. Snaith, M. B. Johnston, L. M. Herz, *Adv. Funct. Mater.* **2015**, *25*, 6218.
- [82] T. Kirchartz, J. Bisquert, I. Mora-Sero, G. Garcia-Belmonte, *Phys. Chem. Chem. Phys.* **2015**, *17*, 4007.
- [83] J. Kang, L. W. Wang, *J. Phys. Chem. Lett.* **2017**, *8*, 489.
- [84] a) D. N. Dirin, L. Protesescu, D. Trummer, I. V. Kochetygov, S. Yakunin, F. Krumeich, N. P. Stadie, M. V. Kovalenko, *Nano Lett.* **2016**, *16*, 5866; b) H. Huang, M. I. Bodnarchuk, S. V. Kershaw, M. V. Kovalenko, A. L. Rogach, *ACS Energy Lett.* **2017**, *2*, 2071; c) W.-J. Yin, T. Shi, Y. Yan, *Appl. Phys. Lett.* **2014**, *104*, 063903; d) W.-J. Yin, T. Shi, Y. Yan, *Adv. Mater.* **2014**, *26*, 4653.
- [85] M. W. Swift, J. L. Lyons, *J. Mater. Chem. A* **2021**, *9*, 7491.
- [86] X. Zhang, M. E. Turiansky, C. G. Van de Walle, *J. Phys. Chem. C* **2020**, *124*, 6022.
- [87] X. Zhang, J.-X. Shen, M. E. Turiansky, C. G. Van de Walle, *Nat. Mater.* **2021**, *20*, 971.
- [88] Z. Liu, J. Siekmann, B. Klingebiel, U. Rau, T. Kirchartz, *Adv. Energy Mater.* **2021**, *11*, 2003386.
- [89] T. Kirchartz, J. A. Marquez, M. Stolterfoht, T. Unold, *Adv. Energy Mater.* **2020**, *10*, 1904134.
- [90] U. Rau, U. W. Paetzold, T. Kirchartz, *Phys. Rev. B* **2014**, *90*, 035211.
- [91] T. Kirchartz, F. Staub, U. Rau, *ACS Energy Lett.* **2016**, *1*, 731.
- [92] D. W. deQuilettes, S. Koch, S. Burke, R. K. Paranj, A. J. Shropshire, M. E. Ziffer, D. S. Ginger, *ACS Energy Lett.* **2016**, *1*, 438.
- [93] a) S. Ravishanker, T. Unold, T. Kirchartz, *Science* **2021**, *371*, eabd8014; b) F. Werner, S. Siebentritt, *Phys. Rev. Appl.* **2018**, *9*, 054047; c) R. A. Awani, Z. Song, C. Chen, C. Li, C. Wang, M. A. Razooqi, L. Chen, X. Wang, R. J. Ellingson, J. V. Li, Y. Yan, *Joule* **2020**, *4*, 644.
- [94] V. M. Le Corre, E. A. Duijnste, O. El Tambouli, J. M. Ball, H. J. Snaith, J. Lim, L. J. A. Koster, *ACS Energy Lett.* **2021**, *6*, 1087.
- [95] J. A. Röhr, T. Kirchartz, J. Nelson, *J. Phys.: Condens. Matter* **2017**, *29*, 205901.

- [96] J. Siekmann, S. Ravishankar, T. Kirchartz, *ACS Energy Lett.* **2021**, *6*, 3244.
- [97] X. Zhang, M. E. Turiensky, J.-X. Shen, C. G. Van de Walle, *Phys. Rev. B* **2020**, *101*, 140101.
- [98] A. Alkauskas, C. E. Dreyer, J. L. Lyons, C. G. Van de Walle, *Phys. Rev. B* **2016**, *93*, 201304.
- [99] X. Zhang, J.-X. Shen, C. G. Van de Walle, *Adv. Energy Mater.* **2020**, *10*, 1902830.
- [100] M. E. Turiensky, A. Alkauskas, M. Engel, G. Kresse, D. Wickramaratne, J.-X. Shen, C. E. Dreyer, C. G. Van de Walle, *Comput. Phys. Commun.* **2021**, *267*, 108056.
- [101] B. Das, Z. Liu, I. Aguilera, U. Rau, T. Kirchartz, *Mater. Adv.* **2021**, *2*, 3655.
- [102] a) W. Chai, J. Ma, W. Zhu, D. Chen, H. Xi, J. Zhang, C. Zhang, Y. Hao, *ACS Appl. Mater. Interfaces* **2021**, *13*, 2868; b) Z. Xu, L. Wang, Q. Han, Y. Kamata, T. Ma, *ACS Appl. Mater. Interfaces* **2020**, *12*, 12867; c) G. F. Samu, Á. Balog, F. De Angelis, D. Meggiolaro, P. V. Kamat, C. Janáky, *J. Am. Chem. Soc.* **2019**, *141*, 10812.
- [103] W. Xiang, S. Liu, W. Tress, *Angew. Chem., Int. Ed.* **2021**, *60*, 26440.
- [104] J. Wang, J. Zhang, Y. Z. Zhou, H. B. Liu, Q. F. Xue, X. S. Li, C. C. Chueh, H. L. Yip, Z. L. Zhu, A. K. Y. Jen, *Nat. Commun.* **2020**, *11*, 177.
- [105] T. Niu, W. Zhu, Y. Zhang, Q. Xue, X. Jiao, Z. Wang, Y.-M. Xie, P. Li, R. Chen, F. Huang, Y. Li, H.-L. Yip, Y. Cao, *Joule* **2021**, *5*, 249.
- [106] W. H. Zhang, J. Xiong, J. H. Li, W. A. Daoud, *Adv. Energy Mater.* **2021**, *11*, 2003585.
- [107] J. J. Tian, J. Wang, Q. F. Xue, T. Q. Niu, L. Yan, Z. L. Zhu, N. Li, C. J. Brabec, H. L. Yip, Y. Cao, *Adv. Funct. Mater.* **2020**, *30*, 10.
- [108] Y. Hou, X. Du, S. Scheiner, D. P. McMeekin, Z. Wang, N. Li, M. S. Killian, H. Chen, M. Richter, I. Levchuk, N. Schrenker, E. Spiecker, T. Stubhan, N. A. Luechinger, A. Hirsch, P. Schmuki, H.-P. Steinrück, R. H. Fink, M. Halik, H. J. Snaith, C. J. Brabec, *Science* **2017**, *358*, 1192.
- [109] X. Sun, B. He, J. Zhu, R. Zhu, H. Chen, Y. Duan, Q. Tang, *Chem. Eng. J.* **2021**, *412*, 128727.
- [110] J. H. Heo, F. Zhang, C. Xiao, S. J. Heo, J. K. Park, J. J. Berry, K. Zhu, S. H. Im, *Joule* **2021**, *5*, 481.
- [111] R. Chen, Y. Hui, B. Wu, Y. Wang, X. Huang, Z. Xu, P. Ruan, W. Zhang, F. Cheng, W. Zhang, J. Yin, J. Li, N. Zheng, *J. Mater. Chem. A* **2020**, *8*, 9597.
- [112] a) Y. Hou, C. Xie, V. V. Radmilovic, B. Puscher, M. Wu, T. Heumüller, A. Karl, N. Li, X. Tang, W. Meng, S. Chen, A. Osvet, D. Guldi, E. Spiecker, V. R. Radmilović, C. J. Brabec, *Adv. Mater.* **2019**, *31*, 1806516; b) M. Yavari, M. Mazloum-Ardakani, S. Gholipour, M. M. Tavakoli, S.-H. Turren-Cruz, N. Taghavinia, M. Grätzel, A. Hagfeldt, M. Saliba, *Adv. Energy Mater.* **2018**, *8*, 1800177; c) N.-G. Park, *Nat. Sustainability* **2021**, *4*, 192.
- [113] a) C. Dong, X. Han, Y. Zhao, J. Li, L. Chang, W. Zhao, *Sol. RRL* **2018**, *2*, 1800139; b) W. Chen, H. Chen, G. Xu, R. Xue, S. Wang, Y. Li, Y. Li, *Joule* **2019**, *3*, 191; c) X. Ding, Y. Zhang, F. Sheng, Y. Li, L. Zhi, X. Cao, X. Cui, D. Zhuang, J. Wei, *ACS Appl. Energy Mater.* **2021**, *4*, 5504.
- [114] H.-Y. Lin, C.-Y. Chen, B.-W. Hsu, Y.-L. Cheng, W.-L. Tsai, Y.-C. Huang, C.-S. Tsao, H.-W. Lin, *Adv. Funct. Mater.* **2019**, *29*, 1905163.
- [115] M. Tai, G. Wang, X. Yin, Y. Zhou, J. Han, Y. Wei, K. Jiang, H. Lin, *Energy Technol.* **2019**, *7*, 1800986.
- [116] Y. Han, H. Zhao, C. Duan, S. Yang, Z. Yang, Z. Liu, S. Liu, *Adv. Funct. Mater.* **2020**, *30*, 1909972.
- [117] J. Liang, C. Wang, Y. Wang, Z. Xu, Z. Lu, Y. Ma, H. Zhu, Y. Hu, C. Xiao, X. Yi, G. Zhu, H. Lv, L. Ma, T. Chen, Z. Tie, Z. Jin, J. Liu, *J. Am. Chem. Soc.* **2016**, *138*, 15829.
- [118] B. Conings, J. Drijkoningen, N. Gauquelin, A. Babayigit, J. D'Haen, L. D'Olieslaeger, A. Ethirajan, J. Verbeeck, J. Manca, E. Mosconi, F. D. Angelis, H.-G. Boyen, *Adv. Energy Mater.* **2015**, *5*, 1500477.
- [119] Q. S. Zeng, X. Y. Zhang, C. M. Liu, T. L. Feng, Z. L. Chen, W. Zhang, W. T. Zheng, H. Zhang, B. Yang, *Sol. RRL* **2019**, *3*, 1800239.
- [120] a) W. Xiang, S. Liu, W. Tress, *Energy Environ. Sci.* **2021**, *14*, 2090; b) D. L. Bai, H. Bian, Z. W. Jin, H. R. Wang, L. N. Meng, Q. Wang, S. Z. Liu, *Nano Energy* **2018**, *52*, 408; c) G. Q. Tong, L. K. Ono, Y. B. Qi, *Energy Technol.* **2020**, *8*, 1900961; d) W. C. Xiang, W. Tress, *Adv. Mater.* **2019**, *31*, 1902851.
- [121] Y. Wang, X. Liu, T. Zhang, X. Wang, M. Kan, J. Shi, Y. Zhao, *Angew. Chem., Int. Ed. Engl.* **2019**, *58*, 16691.
- [122] Y. F. Zheng, X. Y. Yang, R. Su, P. Wu, Q. H. Gong, R. Zhu, *Adv. Funct. Mater.* **2020**, *30*, 9.
- [123] N. Li, Z. L. Zhu, J. W. Li, A. K. Y. Jen, L. D. Wang, *Adv. Energy Mater.* **2018**, *8*, 1800525.
- [124] P. Y. Wang, X. W. Zhang, Y. Q. Zhou, Q. Jiang, Q. F. Ye, Z. M. Chu, X. X. Li, X. L. Yang, Z. G. Yin, J. B. You, *Nat. Commun.* **2018**, *9*, 2225.
- [125] Q. F. Ye, Y. Zhao, S. Q. Mu, F. Ma, F. Gao, Z. M. Chu, Z. G. Yin, P. Q. Gao, X. W. Zhang, J. B. You, *Adv. Mater.* **2019**, *31*, 1905143.
- [126] J. H. Zhang, Z. W. Wang, A. Mishra, M. L. Yu, M. Shasti, W. Tress, D. J. Kubicki, C. E. Avalos, H. Z. Lu, Y. H. Liu, B. I. Carlsen, A. Agarwalla, Z. S. Wang, W. C. Xiang, L. Emsley, Z. H. Zhang, M. Grätzel, W. L. Guo, A. Hagfeldt, *Joule* **2020**, *4*, 222.
- [127] X. J. Wang, X. Q. Ran, X. T. Liu, H. Gu, S. W. Zuo, W. Hui, H. Lu, B. Sun, X. Y. Gao, J. Zhang, Y. D. Xia, Y. H. Chen, W. Huang, *Angew. Chem., Int. Ed.* **2020**, *59*, 13354.
- [128] Y. Q. Zhang, C. C. Wu, D. Wang, Z. H. Zhang, X. Qi, N. Zhu, G. H. Liu, X. D. Li, H. Z. Hu, Z. J. Chen, L. X. Xiao, B. Qu, *Sol. RRL* **2019**, *3*, 1900345.
- [129] J. Liang, P. Y. Zhao, C. X. Wang, Y. R. Wang, Y. Hu, G. Y. Zhu, L. B. Ma, J. Liu, Z. Jin, *J. Am. Chem. Soc.* **2017**, *139*, 14009.
- [130] S. Z. Yang, Z. L. Guo, L. G. Gao, F. Y. Yu, C. Zhang, M. Q. Fan, G. Y. Wei, T. L. Ma, *Sol. RRL* **2019**, *3*, 190104.
- [131] W. S. Subhani, K. Wang, M. Y. Du, S. F. Liu, *Nano Energy* **2019**, *61*, 165.
- [132] Y. L. Wang, K. Wang, W. S. Subhani, C. Q. Zhang, X. Jiang, S. M. Wang, H. X. Bao, L. Liu, L. Wan, S. Z. Liu, *Small* **2020**, *16*, 10.
- [133] Y. Zhao, J. Duan, H. Yuan, Y. Wang, X. Yang, B. He, Q. Tang, *Sol. RRL* **2019**, *3*, 1800284.
- [134] a) M. Stollerfoht, P. Caprioglio, C. M. Wolff, J. A. Márquez, J. Nordmann, S. Zhang, D. Rothhardt, U. Hörmann, Y. Amir, A. Redinger, L. Kegelmann, F. Zu, S. Albrecht, N. Koch, T. Kirchartz, M. Saliba, T. Unold, D. Neher, *Energy Environ. Sci.* **2019**, *12*, 2778; b) L. Krückemeier, B. Krogmeier, Z. Liu, U. Rau, T. Kirchartz, *Adv. Energy Mater.* **2021**, *11*, 2003489; c) J. Wang, W. Fu, S. Jariwala, I. Sinha, A. K. Y. Jen, D. S. Ginger, *ACS Energy Lett.* **2019**, *4*, 222; d) M. Stollerfoht, M. Grischek, P. Caprioglio, C. M. Wolff, E. Gutierrez-Partida, F. Peña-Camargo, D. Rothhardt, S. Zhang, M. Raoufi, J. Wolansky, M. Abdi-Jalebi, S. D. Stranks, S. Albrecht, T. Kirchartz, D. Neher, *Adv. Mater.* **2020**, *32*, 2000080.
- [135] a) D. Luo, R. Su, W. Zhang, Q. Gong, R. Zhu, *Nat. Rev. Mater.* **2020**, *5*, 44; b) S. Akin, N. Arora, S. M. Zakeeruddin, M. Grätzel, R. H. Friend, M. I. Dar, *Adv. Energy Mater.* **2020**, *10*, 1903090; c) F. Gao, Y. Zhao, X. Zhang, J. You, *Adv. Energy Mater.* **2020**, *10*, 1902650.
- [136] B. Li, Y. Zhang, L. Fu, T. Yu, S. Zhou, L. Zhang, L. Yin, *Nat. Commun.* **2018**, *9*, 1076.
- [137] a) Z. F. Liu, L. Kruckemeier, B. Krogmeier, B. Klingebiel, J. A. Marquez, S. Levchenko, S. Oz, S. Mathur, U. Rau, T. Unold, T. Kirchartz, *ACS Energy Lett.* **2019**, *4*, 110; b) J. J. Yoo, S. Wiegbold, M. C. Sponseller, M. R. Chua, S. N. Bertram, N. T. P. Hartono, J. S. Tresback, E. C. Hansen, J.-P. Correa-Baena, V. Bulović,

- T. Buonassisi, S. S. Shin, M. G. Bawendi, *Energy Environ. Sci.* **2019**, 12, 2192.
- [138] Q. Jiang, Y. Zhao, X. Zhang, X. Yang, Y. Chen, Z. Chu, Q. Ye, X. Li, Z. Yin, J. You, *Nat. Photonics* **2019**, 13, 460.
- [139] V. Shrotriya, G. Li, Y. Yao, T. Moriarty, K. Emery, Y. Yang, *Adv. Funct. Mater.* **2006**, 16, 2016.
- [140] J.-F. Guillemoles, T. Kirchartz, D. Cahen, U. Rau, *Nat. Photonics* **2021**, 15, 165.
- [141] a) N. J. Jeon, H. Na, E. H. Jung, T.-Y. Yang, Y. G. Lee, G. Kim, H.-W. Shin, S. Il Seok, J. Lee, J. Seo, *Nat. Energy* **2018**, 3, 682; b) H.-S. Kim, C.-R. Lee, J.-H. Im, K.-B. Lee, T. Moehl, A. Marchioro, S.-J. Moon, R. Humphry-Baker, J.-H. Yum, J. E. Moser, M. Grätzel, N.-G. Park, *Sci. Rep.* **2012**, 2, 591.
- [142] J. A. Röhr, *Phys. Rev. Appl.* **2019**, 11, 054079.
- [143] M. Sajedi Alvar, P. W. M. Blom, G.-J. A. H. Wetzelaer, *Nat. Commun.* **2020**, 11, 4023.
- [144] T. Du, W. Xu, S. Xu, S. R. Ratnasingham, C.-T. Lin, J. Kim, J. Briscoe, M. A. McLachlan, J. R. Durrant, *J. Mater. Chem. C* **2020**, 8, 12648.
- [145] M. Stolterfoht, V. M. Le Corre, M. Feuerstein, P. Caprioglio, L. J. A. Koster, D. Neher, *ACS Energy Lett.* **2019**, 4, 2887.
- [146] a) M. Stolterfoht, C. M. Wolff, Y. Amir, A. Paulke, L. Perdígón-Toro, P. Caprioglio, D. Neher, *Energy Environ. Sci.* **2017**, 10, 1530; b) S. Wheeler, D. Bryant, J. Troughton, T. Kirchartz, T. Watson, J. Nelson, J. R. Durrant, *J. Phys. Chem. C* **2017**, 121, 13496; c) I. Levine, A. Al-Ashouri, A. Musiienko, H. Hempel, A. Magomedov, A. Drevilkauskaitė, V. Getautis, D. Menzel, K. Hinrichs, T. Unold, S. Albrecht, T. Dittrich, *Joule* **2021**, 5, 2915.



Ye Yuan is currently working in the Institute for Energy and Climate at the Forschungszentrum Jülich (FZJ) as a Post-Doc researcher. He received his Ph.D. degree of engineering in 2018 from Sun Yat-sen University (SYSU). Before that, he received his bachelor degree of science in 2013 from SYSU as well. His current research focuses on thin-film photoelectric materials and devices, especially perovskites, $\text{Cu}(\text{In,Ga})\text{Se}_2$, $\text{Cu}_2\text{ZnSn}(\text{S,Se})_4$ and the corresponding physical mechanism.



Genghua Yan graduated in applied physics at Central South University (CSU) in 2013 and completed her Ph.D. in materials physics and chemistry in 2018 at Sun Yat-sen University (SYSU). From 2018–2020, she was a postdoctoral researcher in Department of Physics at Jinan University. She is currently working as a Post-Doc researcher at Forschungszentrum Jülich (FZJ) and SYSU (funded by China and Germany Postdoctoral Exchange Program). Her current research interests include exploring novel thin-film materials and photoelectric devices.



Zongcun Liang is a professor at the Institute for Solar Energy Systems, School of Physics in Sun Yat-sen University (SYSU, since 2006). Previously he was working at Guangzhou Institute of Energy Conversion, Chinese Academy of Sciences (CAS) and as a visiting scholar at Fraunhofer Institute for Solar Energy System, Germany (funded by German Ministry of Aeronautics and Space, 2001–2002). His main research fields are solar cells and device physics as well as photovoltaic materials, including highly efficient crystalline silicon solar cells, novel Si-based heterojunction solar cells, perovskite/Si tandem solar cells, and related new photovoltaic materials.



Thomas Kirchartz is a professor in the Department of Electrical Engineering and Information Technology at the University Duisburg-Essen (since 2013). In addition, he is the head of the department of Analytics and Simulation and the group for Organic and Hybrid Solar Cells at the Research Centre Jülich (Institute for Energy and Climate Research). Previously he was a Junior Research Fellow at Imperial College London (2010–2013) and received a Dr.-Ing. from RWTH Aachen (2009). His research interests include the fundamental understanding of photovoltaic devices, their characterization and simulation and the development of solution-processable solar cells.